Available online at www.sciencedirect.com
SCIENCE DIRECT®
ELSEVIER
European Journal of Mechanics B/Fluids 23 (2004) 319–337
EUROPEAN JOURNAL OF MECHANICS B/FLUIDS

Assessment of common turbulence models for an idealised adverse pressure gradient flow

C.P. Yorke, G.N. Coleman *

School of Engineering Sciences, University of Southampton, SO17 1BJ, UK

Received 8 October 2002; accepted 28 July 2003

Abstract

Results from direct numerical simulation (DNS) of $\mathrm{Re}_\tau = 390$ channel flow subjected to the strain and deceleration typical of adverse pressure gradients (APGs), to the point of skin-friction reversal, are the reference for comparing four simple turbulence models. The statistics satisfy a one-dimensional unsteady problem and contain many of the physical complications associated with APGs, thus allowing a straightforward but nontrivial assessment of the models for APG flows, with rigorously defined boundary and initial conditions and an acceptable Reynolds number. We find the model accuracy varies significantly, with the Spalart–Allmaras and Menter SST schemes giving the best overall agreement with DNS. The other two models tested (Baldwin–Lomax and Launder–Sharma) deviate from the DNS, in terms of skin friction, much the same way they do in actual spatially developing APG boundary layers. This supports the relevance of the strained-channel idealisation. The DNS results are used to examine fundamental assumptions of the four models, casting light on the relative strengths and weaknesses of each.

1. Introduction

The purpose of this study is to compare the predictions of a few popular aerospace turbulence models with results from a recent direct numerical simulation (DNS) of an idealised adverse-pressure-gradient (APG) boundary layer [1,2]. The DNS captures most of the features induced by an APG, and does so in an efficient manner, using an uncomplicated plane-flow geometry with no uncertainty on boundary conditions. The results can also provide insight into the relationship between model performance and APG features that are *absent* from the DNS (such as streamline curvature and detached shear layers), when the idealised-APG predictions are contrasted to previous modeling studies that used actual APG boundary layer data (e.g., [3]). We show below that the DNS represents a non-trivial challenge for the models, and causes them to behave qualitatively as they do in actual APG boundary layers. We thus expect the DNS to be a useful benchmark for model testing and development. In addition, the availability of full Reynolds-stress budgets provides suggestions regarding separate terms, as opposed to mere measurements of the whole-model performance.

2. Approach

2.1. DNS

The DNS emulates a spatially developing low-Mach-number APG boundary layer by simultaneously applying in-plane wall motion and straining the domain of an incompressible turbulent channel flow (Fig. 1). The in-plane wall motion duplicates

* Corresponding author.
E-mail address: g.n.coleman@soton.ac.uk (G.N. Coleman).

0997-7546/$ – see front matter
doi:10.1016/j.euromechflu.2003.07.002

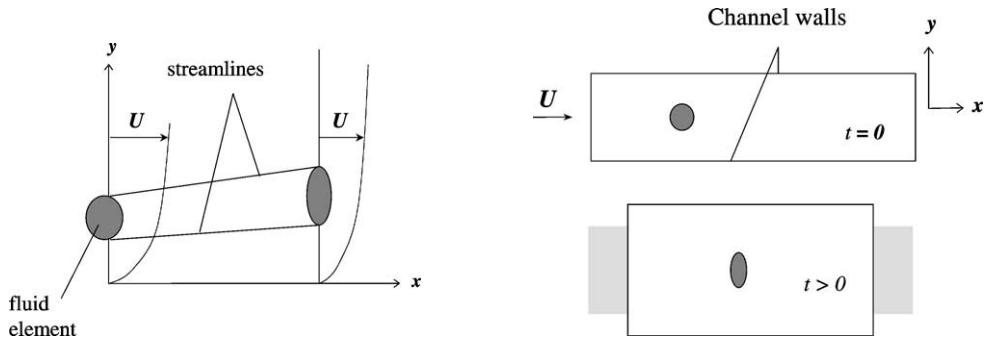

Fig. 1. Side view of 2D APG boundary layer. (a) Spatially developing flow. (b) Initial and deformed domain of time-developing strained-channel idealisation.

the bulk deceleration of the APG, which reduces the wall shear stress, by causing the difference between the mean centerline velocity U_c and wall velocity U_w to decrease. The strain supplies the irrotational plane-strain (streamwise compression with wall-normal divergence) associated with the APG. Deceleration and strain are matched in a plausible sense (see [2] and below). Spatial changes are thus replaced with temporal ones, as the channel turbulence is subjected to the deformation history experienced by boundary-layer fluid in the spatial case (Figs. 1 and 2(a)). The imposed strain field $A_{ij} \equiv \partial U_i/\partial x_j$ is spatially uniform and steps from zero to a constant value at $t = 0$, so that $U_i = A_{ij}x_j$ and $\partial A_{ij}/\partial t = 0$. The components of A_{ij} are associated with a two-dimensional APG, the only nonzero values being the streamwise deceleration $A_{11} \equiv \partial U/\partial x < 0$ and wall-normal divergence $A_{22} \equiv \partial V/\partial y > 0$, with $A_{11} = -A_{22}$. (Other deformations involving spanwise skewing are discussed in [4].) The wall motion $U_w(t)$ is specified such that, when viewed in the reference frame attached to the moving walls, the centerline velocity satisfies $U_c(t)/U_c(0) = \exp(A_{11}t)$, and thus decreases in time at the rate set by the uniform deceleration, $A_{11} < 0$.

This approach has the advantage of producing the desired perturbation in an uncomplicated parallel-flow geometry (see [4] for further details). Since the Reynolds-averaged statistics from the DNS satisfy a one-dimensional unsteady problem, model testing can be done quickly and efficiently, even for models much more complex than the present ones. The features of APG boundary layers captured are the divergence of the outer-layer[1] streamlines and the weakening (and possible reversal) of the mean wall-shear stress τ_w. Missing are streamline curvature and, if the flow separates, the detached/curved shear layers that result from the eruption of the near-wall vorticity. Here, the reversed-flow layer remains very thin.

The DNS is generated by the spectral method described in [4], applied to the case of a relatively weak APG, with $A_{22} = -A_{11}$ chosen to be 31% of $u_\tau(0)/h(0)$, the ratio of the initial friction velocity to the initial channel half-width. The corresponding effective Clauser pressure-gradient parameter $\beta_{\text{eff}} = -\delta^* U_c A_{11}/u_\tau^2$ is initially 0.78; δ^* is the displacement thickness in a half-channel. The Reynolds number $\text{Re}_\tau = u_\tau h/\nu$ of the initial channel flow is 390, which is large enough (roughly four times that needed to sustain turbulence) to produce a well-defined logarithmic layer. The initial Reynolds number based on mean centerline velocity is $\text{Re}_c = U_c h/\nu = 7910$, while the momentum-thickness and bulk Reynolds numbers are respectively $\text{Re}_\theta = U_c\theta/\nu = 703$ and $\text{Re}_m \equiv 2hU_m/\nu = 13\,770$ (θ is the half-channel momentum thickness, and U_m the bulk, wall-to-wall, average velocity.) Mean results have been gathered by averaging over the homogeneous/periodic streamwise and spanwise directions x and z (Fig. 1(b)), doubling the sample by 'folding' about the centerline (invoking symmetry), and this for 21 statistically independent realizations. These were obtained by initiating the strain on the instantaneous fields from 21 distinct times of a preliminary unstrained channel computation. At this Reynolds number, 256 streamwise, 193 wall-normal and 192 spanwise equivalent grid points are required for the Fourier/Chebyshev spectral discretization to capture the full range of turbulent scales [2]. The DNS was performed on Cray T90s at the SCSC/NPACI and DOD/NAVO centers. A total of 2100 single-processor CPU hours was required to obtain the 21-field ensemble, for $0 \leqslant A_{22}t \leqslant 0.365$.

For the present study, the DNS results are the reference data to evaluate the accuracy of selected models, by comparing first- and second-order Reynolds-averaged statistics (Fig. 2). The curves in Fig. 2 represent the DNS data from the 21-field ensemble average, at $A_{22}t = 0$, 0.19 and 0.365; the symbols in Fig. 2(a) and (b) are from a single realization (i.e., x–z plane average and doubling) at $A_{22}t = 0.77$, a time after which a small near-wall reverse-flow region forms. (Second-order statistics for $A_{22}t = 0.77$ are not shown, since they contain large unphysical statistical oscillations due to the incomplete single-field

[1] 'Outer layer' in this context indicates both the wake region of a boundary layer and the 'core' of the channel.

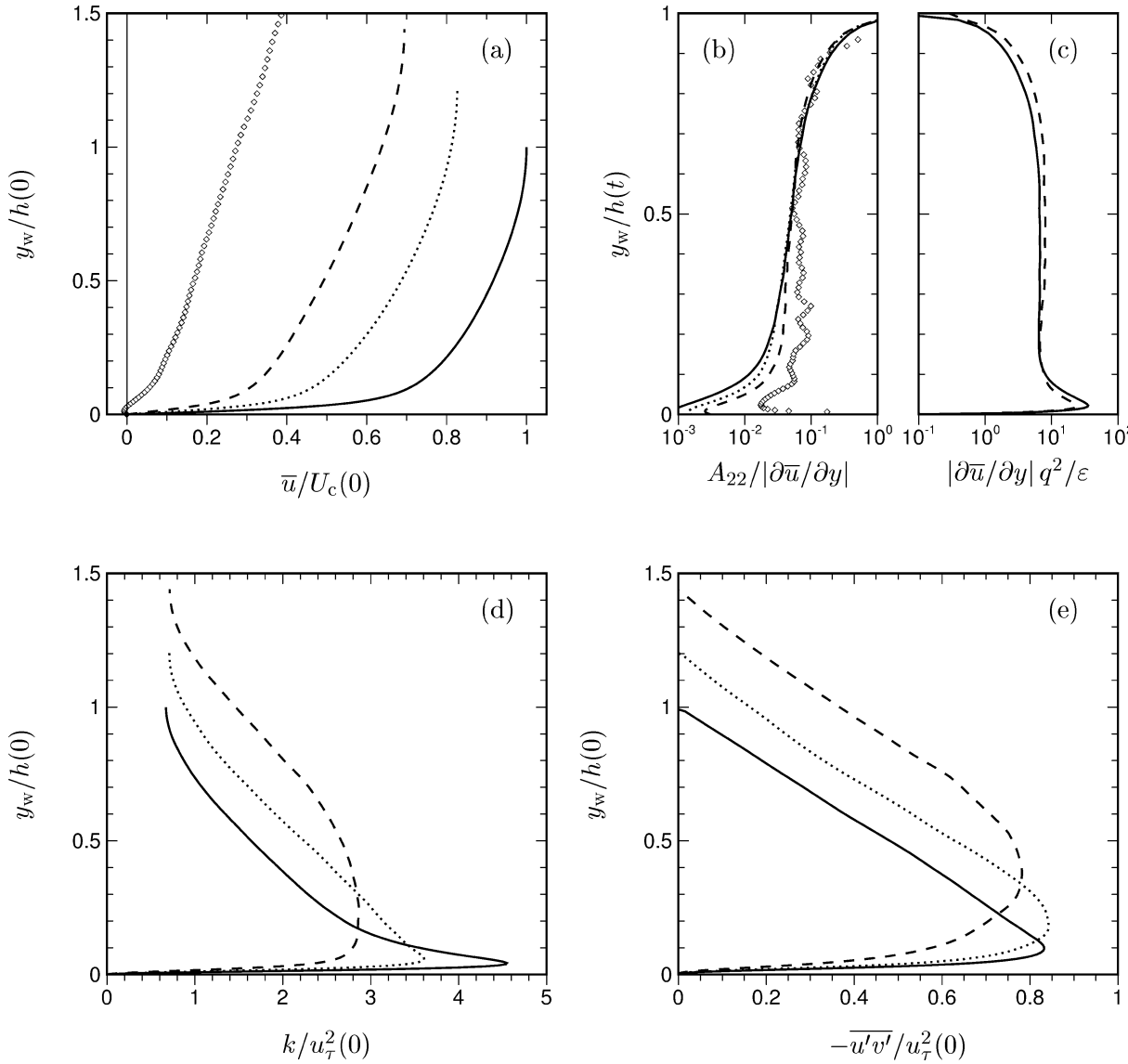

Fig. 2. DNS profiles of (a) mean velocity, (b), (c) timescale ratios, (d) kinetic energy and (e) Reynolds shear stress: —, $A_{22}t = 0$; ⋯, $A_{22}t = 0.19$; - - -, $A_{22}t = 0.365$; ⋄, $A_{22}t = 0.77$ (single realization). The distance to the nearest wall $y_w = |y - h|$.

sample. The cost of extending the full 21-field average up to $A_{22}t = 0.77$, by advancing each of the other 20 DNS realizations from $A_{22}t = 0.365$ to 0.77, would have been of the order of another 2000 T90 CPU hours, which we were unable to justify.)

Many features of APG boundary layers [5,6] are observed in the present flow. These include the increase of layer thickness and reduction of bulk mass flow and wall shear stress, seen in the mean velocity evolution (Fig. 2(a)). The shape factor increases from $H = 1.45$ at $A_{22}t = 0$ to $H = 1.70$ at $A_{22}t = 0.365$ and $H = 2.50$ at $A_{22}t = 0.77$ (just after the skin friction has changed sign; cf. Fig. 10). The latter value is close to the $H \approx 2.7$ found at separation by Alving and Fernholz [7] in their axisymmetric-body separation-bubble experiment. The effective Clauser pressure-gradient parameter β_{eff} increases from $-\delta^* U_c A_{11}/u_\tau^2 = 0.78$ at $A_{22}t = 0$, to 5.7 at $A_{22}t = 0.365$, and then infinity. We are thus far from a constant-β 'equilibrium' regime, for which one could expect similarity of the outer-layer mean-velocity defect [8].

We are also well away from the rapid-distortion regime. Fig. 2(b) shows the relative importance of the applied strain, compared to the mean shear $\partial\overline{u}/\partial y$ at each wall-normal location y_w: A_{22} is at least an order of magnitude smaller than $|\partial\overline{u}/\partial y|$ over the entire channel (except near the centerline, where $\partial\overline{u}/\partial y \to 0$) for all times considered, including just after the wall-shear stress has changed sign. On the other hand, Fig. 2(c) shows that the timescale defined by the mean shear is everywhere

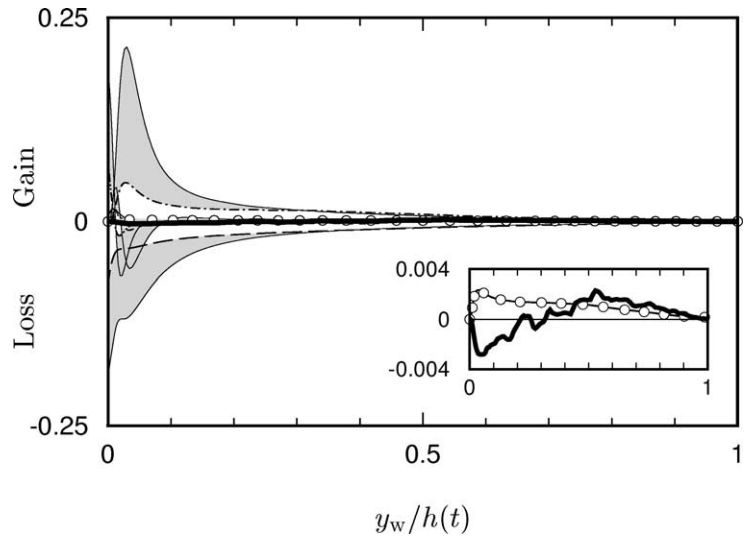

Fig. 3. Terms in turbulence kinetic energy k budget at $A_{22}t = 0.365$: $-\cdot-$, mean-shear production $P_k^S = -\overline{u'v'}\frac{\partial \bar{u}}{\partial y}$; $---$, dissipation $\varepsilon = -\frac{1}{\mathrm{Re}}\overline{\frac{\partial u_i'}{\partial x_\ell}\frac{\partial u_i'}{\partial x_\ell}}$; - - -, turbulent transport; $T_k = -\frac{\partial}{\partial y}(\frac{1}{2}\overline{v'u_i'u_i'})$; $-\cdots-$, viscous diffusion $D_k = \frac{1}{\mathrm{Re}}\frac{\partial^2}{\partial y^2}(\frac{1}{2}\overline{u_i'u_i'})$; $\cdots$, velocity pressure-gradient correlation $\Pi_k = -(\overline{u_i'\frac{\partial p'}{\partial x_i}})$; $\circ$, applied-strain production $P_k^A = -(\overline{u'u'} - \overline{v'v'})A_{11}$ (also shown in inset with expanded vertical scale); thick-solid curve (—), sum of all terms ($\approx \partial k/\partial t$) at $A_{22}t = 0.365$ (also shown in inset). Thin-solid (—) curves denote terms at $t = 0$ (before strain) and are identified by the shaded regions, which indicate change from unstrained initial conditions. Curves normalised by U_{ref}^4/ν, where $U_{\mathrm{ref}} = 1.02u_\tau(0)$ and $\mathrm{Re} = U_{\mathrm{ref}}h(0)/\nu = 400$.

of the same order as the 'eddy turn-over' time q^2/ε (where $k = \frac{1}{2}\overline{u_i'u_i'} = \frac{1}{2}q^2$ is the turbulence kinetic energy and ε its rate of dissipation). The magnitude of the applied strain is thus not large enough, at any y_w, to overwhelm the nonlinear 'self-interaction' processes of the turbulence. This hints at the challenge the present flow provides for one-point closures, since it will for example exercise both the 'rapid' and 'slow' terms in Reynolds-stress transport models.

Other APG characteristics that are duplicated are the near-wall reduction, and outer-layer increase [5], in turbulence intensity, illustrated by the Reynolds shear stress $-\overline{u'v'}$ and turbulence kinetic energy k (Figs. 2(d) and (e)). The effect of the applied strain upon the individual terms in the energy budget is shown in Fig. 3. The near-wall kinetic energy decrease observed in Fig. 2(d) is accompanied by large decreases in both mean-shear production $-\overline{u'v'}\partial\bar{u}/\partial y$ and dissipation ε, with the production falling most rapidly, leading to a negative imbalance (see expanded-scale inset in Fig. 3). The net positive $\partial k/\partial t$ in the outer layer can be traced directly to the applied-strain production $-(\overline{u'u'} - \overline{v'v'})A_{11}$ (denoted by the open symbols in Fig. 3). We examine below the ability of two two-equation models to duplicate the strain-induced behaviour of the production, dissipation and diffusion terms in the turbulence kinetic energy budget.

2.2. Turbulence models

Four models are tested. They include the Baldwin–Lomax (BL) algebraic model [9,10], the Spalart–Allmaras (SA) one-equation eddy-viscosity transport model [11,12,10], the Launder–Sharma (LS) low-Reynolds-number k–ϵ model [13,12,10], and the Menter Shear-Stress Transport (SST) model [14,12]. These were chosen for their current or historical relevance to aerospace CFD applications (other closures, such as the Johnson–King half-equation [15] scheme and various versions of the Wilcox k–ω [16,10] and k–ϵ [17,18] models will also be briefly considered).

The BL (1978) model is a generalisation of the Cebeci–Smith (CS) [19] two-layer mixing-length closure; it was developed to circumvent difficulties associated with computing integral boundary-layer quantities in the CS outer-layer model (edge velocity U_e and displacement thickness δ^*) in complex flows. This was done by using the mean vorticity profile to define the boundary-layer thickness, and by replacing the $U_e\delta^*$ product by a wake function F_{wake}, which depends on the product of the mixing length and the vorticity. BL has received widespread use in the aerospace community, due to its elegance and simplicity, and presumably the priority its creators placed on meeting the needs of the user. It is widely known to give imperfect results for complex flows, especially with regard to separation [10].

The SA (1994) model, based on an empirical transport equation for eddy viscosity ν_T and prompted by the work of Baldwin and Barth [20], has also been heavily influenced by the perceived needs of the user, who is assumed to be primarily concerned

with aerodynamic flows. The ν_T equation was thus tuned to the behaviour of 2D mixing layers and wakes, and 2D flat-plate boundary layers at high and finite Reynolds numbers. The transported dependent variable, which reduces to ν_T far from walls, has the important property of being no more difficult to resolve than the mean velocity in the viscous and inertial sublayers. These 'aerospace-CFD-user-friendly' features, coupled with the fact that a one-equation model is the simplest possible complete closure (i.e., one whose logic or constants does not change from flow to flow), have lead to the widespread use of SA throughout the CFD community. It is subject to the limitations inherent in all eddy-viscosity schemes (e.g., the formal inconsistency that, in reality, the principal axes of the Reynolds-stress and mean-strain-rate tensors are not aligned), and has not performed well for plane and round jet flows [10]. Some observers also perceive difficulties for complex geometries associated with specifying the distance to the nearest wall, which affects the destruction term and the near-wall modification of the production term [21].

The LS (1974) two-equation k–ϵ model is often viewed as the industrial standard CFD closure. It is noteworthy for its use of near-wall damping functions to alter the standard $\nu_T \sim k^2/\varepsilon$ profile in the viscous/buffer layers and to remove the singularity in the ε equation [22,10]. As a consequence of the damping, the scheme suffers from numerical stiffness in the near-wall region. Despite its popularity, it has a number of problems, including predicting late (or nonexistent) separation [12].

The SST (1994) model is a two-equation k–ϵ/k–ω hybrid cast in the form of a k–ω scheme. Menter's motivation was to improve performance for APG and separated boundary layers, and to remove the spurious sensitivity to freestream boundary conditions of the k–ω model. It addresses the former by using an eddy-viscosity limiter, even though the k–ω model is already superior to the k–ϵ model in that respect. The latter is done by blending k–ω and k–ϵ such that k–ω is in effect near the walls (thereby avoiding difficulties with near-wall singularities and damping-functions in the ε equation), while in the outer region k–ϵ (which does not suffer from the freestream boundary condition sensitivity) comes into effect. The SST closure has also become quite popular in aerospace CFD. However, in addition to the inherent eddy-viscosity limitation mentioned above, SST also leaves room for improvement in its predictions of wake flows [12].

Numerical solutions were produced with each model for the mean streamwise velocity $\bar{u}(y,t)$ under the unsteady parallel-flow conditions of the strained channel. The governing and modeling equations are most straightforward when written in terms of new independent variables (η,λ), where $\eta(y,t) = \exp(-A_{22}t)y = b(t)y$ and $\lambda(y,t) = t$. In these 'deforming coordinates' (see [4] and Appendix), the mean streamwise momentum equation is

$$\frac{\partial \bar{u}}{\partial \lambda} = -A_{11}\bar{u} + b(\lambda)\frac{\partial}{\partial \eta}\left[\nu b(\lambda)\frac{\partial \bar{u}}{\partial \eta} - \overline{u'v'}\right], \tag{1}$$

subject to the boundary conditions $\bar{u}(\eta,\lambda) = U_w(\lambda)$ at $\eta = \pm h(0)$, where

$$U_w(\lambda) = U_c(\lambda) - U_c(0)\exp(A_{11}\lambda). \tag{2}$$

The wall velocity $U_w(\lambda)$ is dynamically adjusted in response to the current value of the mean centerline velocity $U_c(\lambda)$, which is itself affected by the strain. (In practice, where a finite-difference time-marching scheme is employed, we use an explicit approximation to set U_w at the next time level.) In the reference frame attached to the moving walls this gives $U_c(\lambda) = U_c(0)\exp(A_{11}\lambda)$, and thus provides the bulk deceleration appropriate for an APG. Note also that as a result of the straining, the channel half-width h increases with time as $h(\lambda) = h(0)\exp(A_{22}\lambda)$ (while in the deforming η, λ coordinates the walls remain at $\eta = \pm h(0)$). We invoke symmetry and solve the momentum and model equations over the half-channel domain, $y_w \in [0, h(0)]$, and impose zero-slope boundary conditions at the centerline on $\bar{u}$ and the model transport variables (see Appendix).

Eq. (1) and the relevant model equations are solved using a modified version of a finite-difference code ('Pipe.f') originally written by Wilcox [10] for the steady-state unstrained plane channel. The original and strained-channel codes use a second-order Crank–Nicolson discretization in y (now η) and include a range of turbulence models, including some of those tested below. (The k–ϵ, SST and Johnson–King models were added by the authors.)

The conversion from fixed- to strained-channel geometry requires (i) replacing the iterative relaxation-to-steady-state method with a fixed-step time-accurate scheme, (ii) adding the A_{ij} terms in (1) and the model equations, (iii) multiplying all y derivatives by the time-dependent metric $b(t) = \exp(-A_{22}t)$, (iv) dividing the wall-normal distance y_w (in models that use it) by $b(t)$ to account for the strain-induced stretching of the domain, and (v) prescribing the time-dependent in-plane motion of the walls (2). (Coding of the Spalart–Allmaras solution in Pipe.f also needed correction.) Details of the four models are presented in Appendix, showing the form they take in the deforming (η,λ) coordinates.

We utilise 400 grid points between the wall and the channel centerline for each model, and integrate through the viscous sublayer. A geometric grid stretching monotonically clusters the points near the wall, with the first grid point 0.12 initial wall units above the wall for all four models. A fixed time step of 1.25×10^{-2} initial wall units was found to be sufficiently small for all but the SST run, which required 3.125×10^{-3}. These values of grid and time step produce grid-independent results. The model tests were made on an 800 MHz Pentium III PC. The 275 000 steps required by the SST run to achieve negative wall shear stress (see Fig. 10) took approximately 9 minutes. Well-defined initial conditions were obtained from the steady-state version of the code (Pipe.f), and it was checked that the unsteady code maintained these solutions with the strain set to zero.

3. Results

3.1. Unstrained plane-channel flow

Before considering the APG effects, we use the unstrained initial conditions to test how well each model is able to predict $\mathrm{Re}_\tau = 390$ ($\mathrm{Re}_\theta \approx 703$, $\mathrm{Re_m} \approx 13\,770$) 2D plane-channel flow. (Wilcox did the same for another set of models in [10]; see also Chapter 6 of Durbin and Pettersson Reif [22].) Note that each model imposes $\mathrm{Re}_\tau \equiv 390$, so that variations of U_c/u_τ and U_m/u_τ begin to indicate the global accuracy for each model. We find that all four approximate u_τ^2/U_c^2 to within 10% of the DNS value of 0.00245, which corresponds to $C_f = \tau_\mathrm{w}/\frac{1}{2}\rho U_\mathrm{m}^2 = 6.47 \times 10^{-3}$. (This C_f is within 1% of that given by Halleen and Johnston's [23] experimental correlation, $C_f = 0.0706\,\mathrm{Re_m}^{-1/4}$, and within 4% of the Dean relation [24], $C_f = 0.073\,\mathrm{Re_m}^{-1/4}$.) Results are summarised in Table 1. The corresponding modelled mean velocities are shown in Fig. 4, and compared to the DNS results (the solid curve). Since all the models assume the same Re_τ, they must all agree at and very near the wall (Fig. 4(a)). Away from the wall, the exaggerated wake assumed by the BL closure is responsible for its consistent under-prediction of the (smaller-wake) channel-flow profile, which is emphasised by the U_c normalisation used in Fig. 4(b). (When nondimensionalised by U_m, the BL and DNS profiles match near $y_\mathrm{w} = 0.5h$, with the modelled $\bar{u}/U_\mathrm{m}$ near the centerline a few percent larger than the DNS.) This under-prediction is reflected in a slightly too-large shape factor $H = \delta^*/\theta$ (compared to the DNS value of $H = 1.45$) for the BL solution (Table 1). The indifferent performance of the BL model is understandable, given that it was not designed with channel flow in mind, but rather tuned to external boundary layers. It is included here primarily because of its very wide use. In fact the SA and SST models were also tuned in boundary layers, but their use of transport equations with diffusion across the centerline appears to help them better adapt to the channel.

Table 1
DNS and model predictions of unstrained plane channel at $\mathrm{Re}_\tau = 390$ ($A_{22}t = 0$)

Case	u_τ^2/U_c^2	$U_\mathrm{m}/U_\mathrm{c}$	δ^*/h	H	α_eff
DNS	0.00245	0.871	0.129	1.45	0.0305
BL	0.00223	0.850	0.150	1.49	0.0179
SA	0.00251	0.883	0.117	1.45	0.0399
LS	0.00220	0.881	0.119	1.48	0.0369
SST	0.00265	0.887	0.113	1.49	0.0610

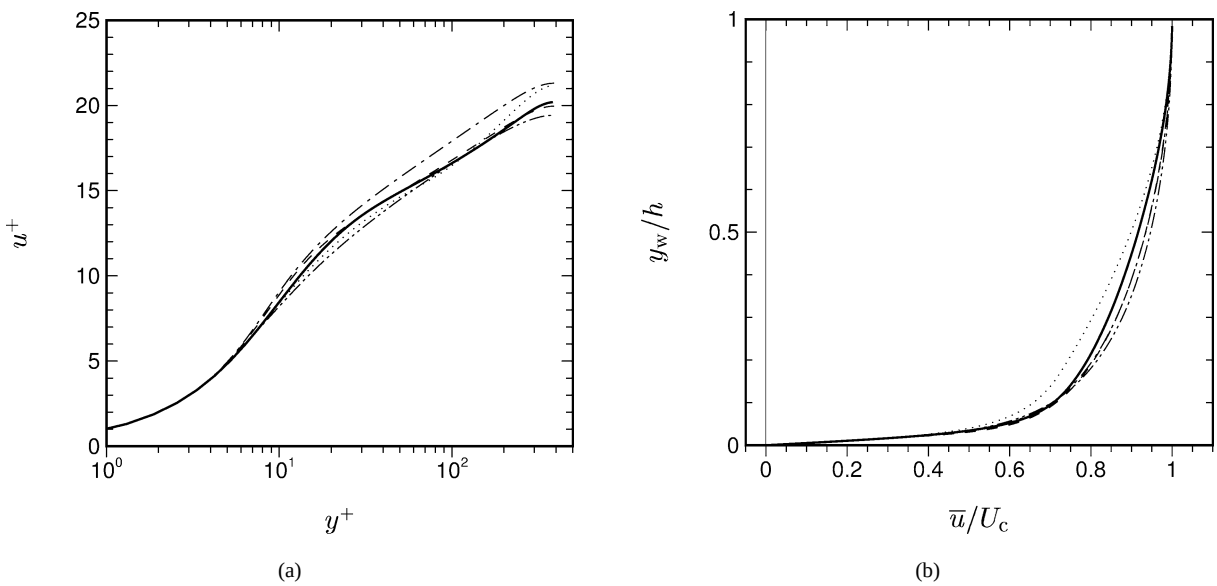

Fig. 4. DNS and model predictions of mean velocity in (a) inner and (b) outer scaling at $A_{22}t = 0$: —, DNS; ⋯, BL; - - -, SA; —·—, LS; —⋯—, SST. (SA and LS in (b) are coincident in outer layer.)

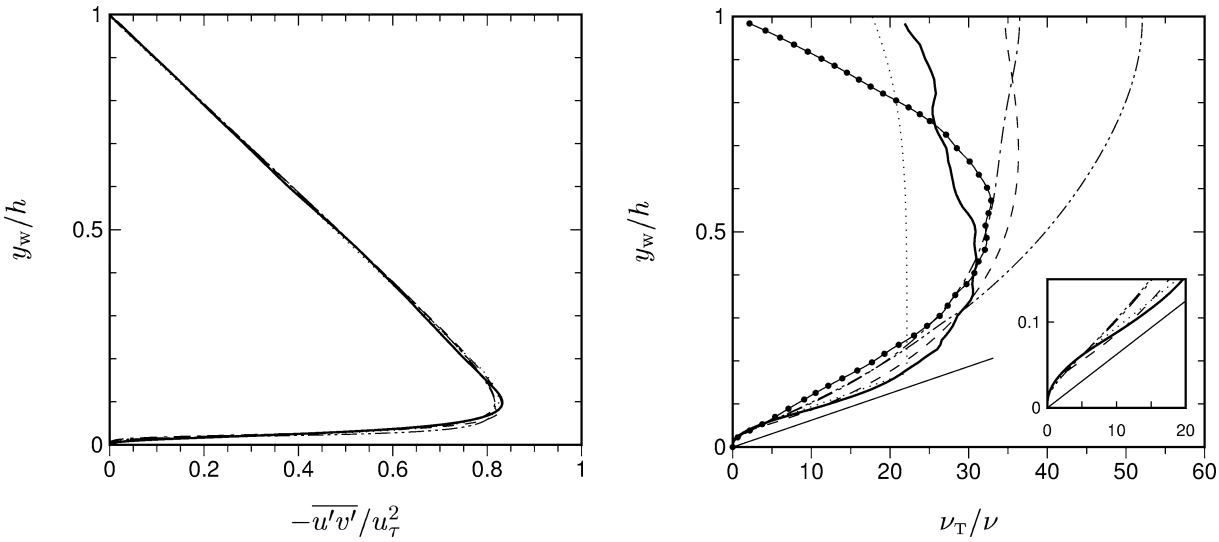

Fig. 5. DNS and model predictions of (a) Reynolds shear stress and (b) eddy viscosity at $A_{22}t = 0$: —, DNS; $\cdots$, BL; - - -, SA; $-\cdot-$, LS; $-\cdot\cdot-$, SST; •, Nikuradse/van Driest pipe-flow mixing-length correlation [26]. Straight-line segment in (b) denotes $\nu_T = \kappa y_w u_\tau$ from DNS (using $\kappa = 0.41$).

The SA result gives the best overall agreement with $\bar{u}$ from the DNS, when each of the U_c, U_m and especially the u_τ (Fig. 4(a)) normalisations are considered; next best is LS, which in both outer-layer scalings (U_c and U_m) is indistinguishable from the SA profile. The $U_c - \bar{u}$ defect from SST is consistently a few percent too small in the outer layer.

The model representations of the Reynolds shear stress $-\overline{u'v'}$ are all quite good (Fig. 5(a)), although the combination of the u_τ scaling and the linear outer-layer profile required of *any* steady-state plane-channel solution minimises the discrepancies. The LS $-\overline{u'v'}$ peak is the least accurate, being too small by 2% – which is not unreasonable, especially considering that the peak in the k profile for this model (not shown) is 32% smaller than the k from the DNS. Michelassi et al. [25] have suggested that the diminished peak k is primarily due to the eddy-viscosity wall damping term f_μ; we show below that it has more to do with the near-wall behaviour of ε.

The mean velocity is driven by each model's eddy viscosity (Fig. 5(b)). Although they agree closely near the wall (especially for $y_w < 0.08h \approx 30\nu/u_\tau$; see Fig. 5(b) inset), with each other and with $-\overline{u'v'}/(\partial\bar{u}/\partial y)$ from the DNS, large discrepancies occur in the outer layer. These are quantified in Table 1 in terms of an effective outer-layer Clauser coefficient $\alpha_{\text{eff}} \equiv \nu_{T,\max}/U_c\delta^*$, where $\nu_{T,\max}$ is the largest ν_T for each case (which for LS and SST occurs at the channel centerline). None of the α_{eff} from the models is particularly close to the DNS. This was expected for BL, designed as it was to reproduce external boundary layers and their large wakes; its $\alpha_{\text{eff}} = 0.0179$ is close to the standard boundary-layer value of 0.0168 (the difference is due to the approximation in BL of $U_c\delta^*$ by the wake function F_{wake}). Some of the disparity between the BL and DNS α_{eff} might also be due to low Reynolds number: when the Cebeci–Smith Re_θ correction [19] is applied, the effective outer-layer Clauser coefficient increases from 0.0179 to 0.024, which is within 22% of the $\alpha_{\text{eff}} = 0.0305$ from the DNS. The slight drop in the BL ν_T as $y_w \to h$ indicates the minimal effect the Klebenoff intermittency function F_{Kleb} has for this flow. One could argue on physical grounds that there should be *no* intermittency effect in the channel, with $F_{\text{Kleb}} = 1$. We have nevertheless chosen to use the 'off-the-shelf' version of BL [10].

Surprisingly, other than avoiding the inner/outer-layer slope discontinuity, the one- and two-equation ν_T predictions do not provide much if any improvement over the algebraic model over the region $y_w/h > 0.4$. In fact, they do no better than the empirical Nikuradse/van Driest mixing-length correlation for pipe flow[2] (indicated by the symbols in Fig. 5(b)). The SST model (which for the unstrained channel reduces to the k–ω closure [16], with the k–ω/k–ϵ blending function $F_1 = 1$ everywhere), in particular differs from the DNS by as much as 100%. Comparing model results with the recent computations of Hu and Sandham [27], we find the same general trends hold at $\text{Re}_\tau = 720$: the BL ν_T is again about 20% smaller than the DNS in the

[2] I.e., $\nu_T = \ell_*^2|\partial\bar{u}/\partial y|$, where $\ell_* = \ell[1 - \exp(-y^+/A^+)]$, $A^+ = 26$, and ℓ is given by Eq. (20.18) of [26], with $\partial\bar{u}/\partial y$ taken from the DNS data.

outer layer, SST as much as 100% too large (with its maximum at $y_w = h$), and SA and LS fall roughly halfway between the SST and DNS profiles.

The Nikuradse ℓ_{mix} curve is also shown in Fig. 6, where it is compared with the $(-\overline{u'v'})^{1/2}/(\partial\bar{u}/\partial y)$ ratio from the DNS. The good agreement is a symptom of the simplicity of this steady parallel shear flow, for which a mixing-length closure is adequate. Fig. 6 also supports the use for this flow of the standard zero-pressure-gradient van Driest damping coefficient ($A_0^+ = 26$) in the BL scheme (see dotted curve in inset). In the outer layer, the DNS results suggest that at least for the plane channel it is slightly better to assume a constant ν_T than a constant ℓ_{mix} (cf. Figs. 5(b) and 6).

The excess outer-layer ν_T for SA can be remedied by altering the destruction term, which along with the production and diffusion is plotted in Fig. 7(a) (see Appendix for definitions). Note that the channel geometry (and the form of the diffusion term used; see Appendix), precludes the existence of any ramp/front-type behaviour that can appear in the SA solutions at a boundary-layer/freestream interface [11]. (The nonzero destruction and diffusion near the centerline are due to the fact that at

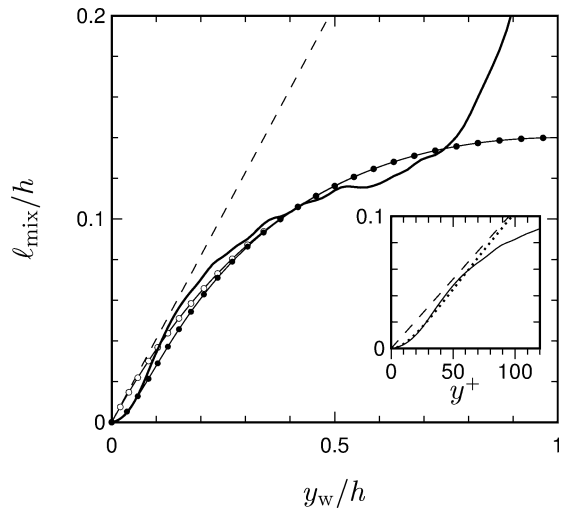

Fig. 6. Mixing-length ℓ_{mix} profiles at $A_{22}t = 0$: —, $(-\overline{u'v'})^{1/2}/(\partial\bar{u}/\partial y)$ from DNS; - - -, κy_w ($\kappa = 0.41$); $\cdots$, $\kappa y_w(1-\exp(-y_w/A_0^+))$, with $\kappa = 0.41$ and $A_0^+ = 26$; ∘, Nikuradse (Eq. (21.18) of [26]); •, Nikuradse with $A_0^+ = 26$ van Driest damping.

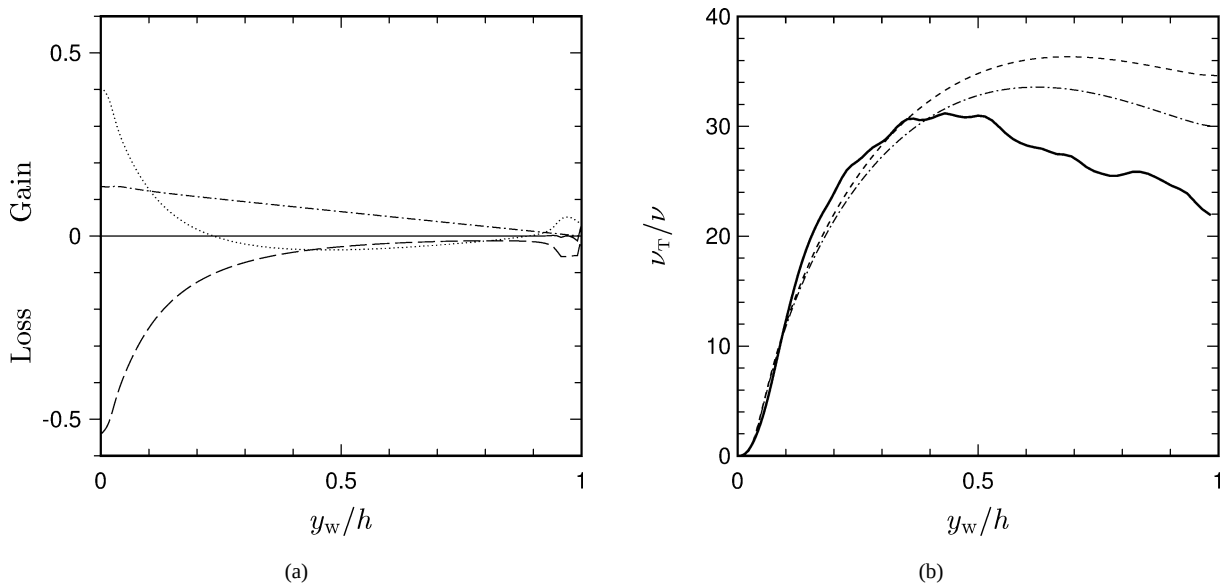

Fig. 7. (a) Terms in SA budget at $A_{22}t = 0$: $-\cdot-$, production; $---$, destruction; $\cdots$, diffusion; —, $\partial\tilde{\nu}/\partial t$ (see Appendix). (b) Profiles of ν_T at $A_{22}t = 0$: —, DNS; - - -, SA; $-\cdot-$, SA with modified distance-to-wall $\mathcal{D} = (2h/\pi)\sin(\pi y_w/2h)$ in destruction term.

$y_w = h$, both $\partial\bar{u}/\partial y \equiv 0$ and $\partial\tilde{v}/\partial y = 0$ (so that ν_T remains finite), which leads to a nonzero (but finite) value of the wall function f_w multiplying the destruction term [11].) An improvement to the SA ν_T prediction can be obtained by accounting for the finite width of the channel, and the dual wall-normal distances when evaluating the destruction term (which is proportional to $(\nu_T/y_w)^2$). In the spirit of Fares and Schröder [21], we replace y_w with a smoothed 'distance function' $\mathcal{D}$ whose slope $d\mathcal{D}/dy$ is 1 at the wall and 0 at the centerline (i.e., using, in the Fares and Schröder notation, a nonzero σ in order to remove the singularity in the slope at the midpoint between two plane walls). We approximate the $\sigma = 1$ solution to the elliptic partial differential equation for $\mathcal{D}$ (see their Fig. 2), by replacing y_w in the SA destruction term with $\mathcal{D} = (2h/\pi)\sin(\pi y_w/2h)$. This results in essentially no change to the individual terms in the SA budget in Fig. 7(a), but does lead to a sizeable reduction in ν_T ($\sim \mathcal{D} \cdot \text{destruction}^{1/2}$) in the outer layer (the chain-dot curve in Fig. 7(b)). This in turn somewhat improves the prediction of all of the quantities listed in Table 1. For example, δ^*/h becomes 0.121 (compared to 0.117) and α_{eff} is now 0.0355 (instead of 0.0399) – both closer to the DNS values of 0.129 and 0.0305, respectively.

Fig. 8 illustrates the behaviour of terms involved in the LS eddy-viscosity, given by $\nu_T = C_\mu f_\mu k^2/\tilde{\varepsilon}$, where $f_\mu = \exp(-3.4/(1 + \text{Re}_T/50)^2)$ is the LS damping function, with $\text{Re}_T = k^2/\tilde{\varepsilon}\nu$, and $C_\mu = 0.09$. The LS dissipation variable $\tilde{\varepsilon}$ is the difference between the actual dissipation ε and $\varepsilon_0 \equiv 2\nu(\partial k^{1/2}/\partial y)^2$; since ε_0 and ε are equal at the wall, $\tilde{\varepsilon}$ goes to zero there (see dotted curve in Fig. 8(a)). The agreement between the LS solutions for $\tilde{\varepsilon}$ and ε in Fig. 8(a) and the corresponding quantities from the DNS (solid curves) is not especially good. The model's damping function (Fig. 8(b)) is also significantly different from that deduced from the DNS. The $C_\mu f_\mu$ profile used by the LS solution (chain-dotted curve) is much larger near the wall than the ratio of the DNS variables $-\overline{u'v'}/(\partial\bar{u}/\partial y)/\{k^2/[\varepsilon - 2\nu(\partial k^{1/2}/\partial y)^2]\}$ (solid curve). The difference is even greater when the LS damping $C_\mu f_{\mu(\text{Re}_T)}$ is evaluated using the $\text{Re}_T = k^2/\tilde{\varepsilon}\nu$ distribution from the DNS (dashed curve). When viewed in light of the ν_T and $\tilde{\varepsilon}$ results presented above, this implies that the diminished peak k (mentioned earlier, which occurs near $y_w = 0.055h$, $y^+ = 22$) predicted by LS is not due to excess damping by f_μ (cf. [25]) – since the model damping goes to zero as $y_w \to 0$ much slower than the DNS profile does – but rather to the spurious extra dissipation just above the wall observed in Fig. 8(a) (see also Fig. 9(a)). However, as we have already seen from Fig. 5(b), despite these formal inconsistencies reasonable near-wall values of ν_T are obtained from the k, ε and f_μ solutions given by LS for the stationary channel flow (we shall find below however that this is not the case for the strained flow). In fact, some two-equation modellers prefer not to view k as the actual turbulence kinetic energy,[3] but solely as a dependent variable used to set the velocity scale in the ν_T formula. This perspective is validated by the good agreement between the production term in the k LS model equation and the k budget from the DNS, which are compared in Fig. 9(a) – especially when the large discrepancies between the model and the DNS for both the transport and dissipation terms are taken into account.

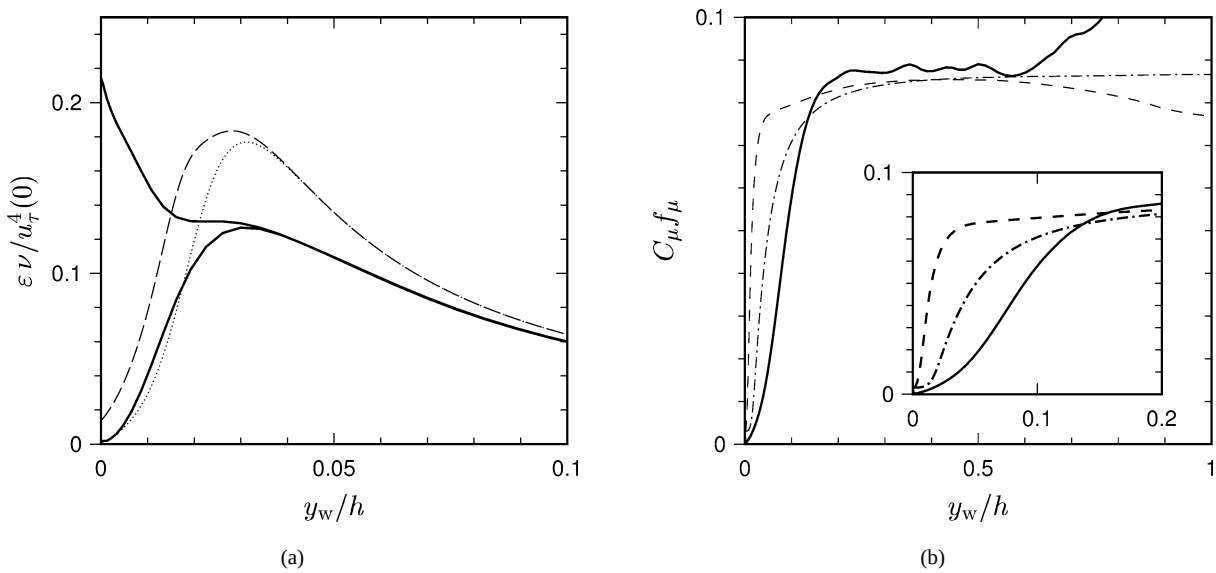

Fig. 8. (a) Dissipation rate ε profiles for LS at $A_{22}t = 0$: $\cdots$, $\tilde{\varepsilon}$; $---$, ε; —, $\tilde{\varepsilon}$ and ε from DNS. (b) Eddy-viscosity damping for LS at $A_{22}t = 0$: —, $\nu_T\tilde{\varepsilon}/k^2$ from DNS; - - -, $C_\mu \exp(-3.4/(1 + \text{Re}_T/50)^2)$, using $\text{Re}_T = k^2/\tilde{\varepsilon}\nu$ from DNS; $-\cdot-$, $C_\mu \exp(-3.4/(1 + \text{Re}_T/50)^2)$, using $\text{Re}_T = k^2/\tilde{\varepsilon}\nu$ from k and $\tilde{\varepsilon}$ predicted by LS. The LS variable $\tilde{\varepsilon} \equiv \varepsilon - \varepsilon_0$ with $\varepsilon_0 = 2\nu(\partial k^{1/2}/\partial y)^2$.

[3] This is the reason we have not explicitly compared the LS and SST k profiles to the DNS.

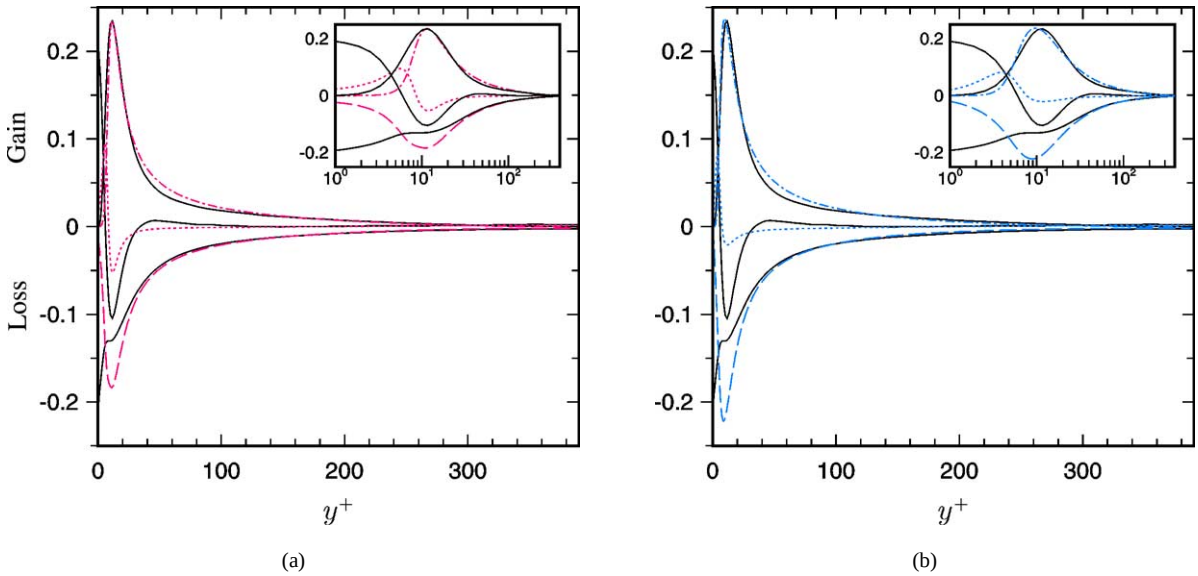

(a) (b)

Fig. 9. DNS and modelled terms in turbulence kinetic energy budget for (a) LS and (b) SST at $A_{22}t = 0$: $-\cdot-$, production P_k^S; $---$, dissipation $-\varepsilon$; $\cdots$, diffusion $T_k + D_k + \Pi_k$; —, DNS. See Fig. 3 caption for definition of budget terms. Curves normalised by $u_\tau^4(0)/\nu$.

The tendency for compensating errors to yield an accurate eddy viscosity from inaccurate constituents is also demonstrated by the SST scheme, whose model-versus-DNS k budget comparison is shown in Fig. 9(b). Again we see the best agreement occurs for the production term, with large differences in magnitude and shape near the wall for the diffusion and dissipation profiles. Here both ν_T and ε are modelled in terms of k and the second variable ω (which can be interpreted as the inverse timescale of the mixing process induced by the dominant eddies [10]), with $\nu_T = k/\omega$ and $\varepsilon = \beta^* k\omega$ (where $\beta^* = 0.09$). Although the representation of ε is rather poor, compared to the DNS, that for the (more important) production term is much better, reflecting the quality of the mean velocity and shear stress predictions observed above.

3.2. Strained-channel flow

Our primary focus is the ability to capture APG effects, and in particular the time at which the wall shear stress τ_w changes sign. Although the $\tau_w = 0$ time is not related to a physical separation, in the sense of a flow departing from the surface at a point in space, we assume that the ability of a model to capture the cumulative effect of the APG by accurately predicting this time indicates its accuracy for attached and separated APG flows of engineering interest.

The skin-friction histories from the DNS and the four models are compared in Fig. 10. The DNS curve is an interpolant through individual realizations [28,2], given by

$$\tau_w(\sigma)/\tau_w(0) = \exp(c_0\sigma) + c_1\sigma^3 + c_2\exp(c_3\sigma)\sin(c_4\sigma), \tag{3}$$

where $\sigma = A_{22}t$ and $(c_0, c_1, c_2, c_3, c_4) = (-3.5433, -0.3127, 2.9267, -29.5295, -3.3553)$. The wall-stress reversal occurs at $A_{22}t = 0.675$. The estimated uncertainty in this value is $\pm 5\%$ (see [28,2]).

The least complex model, BL, significantly under-predicts the separation time, giving $A_{22}t \approx 0.38$. This improves somewhat when the outer-layer formulation is adapted to the channel geometry and low Re_θ, by increasing the Clauser constant from 0.0168 to 0.0286 (such that initially $\alpha_{\mathrm{eff}} \approx 0.305$; see Fig. 5(b), Table 1), to the point that separation is delayed until $A_{22}t \approx 0.45$ (but still well before the DNS value of 0.675). Further improvement would result from other *ad hoc* modifications (we verified for example that decreasing the van Driest damping had the expected effect of delaying the τ_w sign reversal, in line with the Cebeci–Smith pressure-gradient correction for A^+ [8,10]), but the rewards would be small in the current state of CFD. For now we note that the behaviour of the BL model for the APG-strained channel is qualitatively the same as that found in Menter's modeling study [3] of Driver's separation-bubble experiment [29], for which BL also predicted a premature separation. This suggests that the DNS contains at least some of the difficulties with which models must deal in order to perform well when applied to more complex aerodynamic flows. Curiously, shock-induced separation tends to occur too late with BL, possibly distinguishing between gradual and steep pressure variations [30].

The well-known tendency for the LS model to delay separation or even miss it altogether (see [12] for example) is also revealed in the present flow, by the chain-dotted curve in Fig. 10. The LS τ_w does not become negative until $A_{22}t \approx 1.1$. (Other

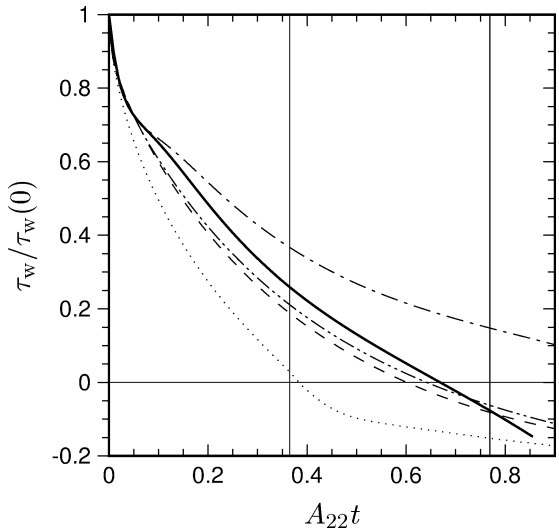

Fig. 10. DNS and model histories of wall shear stress, for $\mathrm{Re}_\tau(0) = 390$ and $A_{11} = -A_{22} = -0.31u_\tau(0)/h(0)$: ⋯, Baldwin–Lomax (BL); - - -, Spalart–Allmaras (SA); $-\cdot-$, Launder–Sharma k–ϵ (LS); $-\cdot\cdot-$, Menter SST; —, interpolant of DNS results [2]. Vertical lines mark times for which mean profiles are shown in Figs. 11–13.

Table 2
DNS and model predictions at $A_{22}t = 0.365$ [$U_c = 0.694U_c(0)$; $h = 1.44h(0)$]

Case	u_τ^2/U_c^2	U_m/U_c	δ^*/h	H	α_{eff}
DNS	0.00128	0.767	0.233	1.70	0.0230
BL	0.00013	0.770	0.230	1.80	0.0223
SA	0.00098	0.804	0.196	1.64	0.0292
LS	0.00168	0.791	0.210	1.67	0.0277
SST	0.00116	0.811	0.189	1.71	0.0383

Table 3
DNS (one sample) and model predictions at $A_{22}t = 0.77$ [$U_c = 0.465U_c(0)$; $h = 2.15h(0)$]

Case	u_τ^2/U_c^2	U_m/U_c	δ^*/h	H
DNS	−0.0001	0.61	0.39	2.5
BL	−0.00156	0.666	0.334	2.39
SA	−0.00096	0.690	0.310	2.19
LS	+0.00152	0.680	0.320	2.08
SST	−0.00077	0.692	0.308	2.30

forms of the k–ϵ model [17,18] behave much differently, predicting both early and late separation.) We again take the similar model behaviour for actual spatial APG boundary layers and the present flow as support for the relevance of the strained-channel idealisation.

Of the four candidates, the best predictions of the $\tau_w = 0$ time are given by the SA ($A_{22}t = 0.60$) and especially the SST ($A_{22}t = 0.64$) models. It is interesting that the SST scheme does this well, despite the fact that the eddy-viscosity limiter (a feature designed to increase the accuracy of separation predictions) has only a minimal effect during the APG strain; at no time is $\nu_T < 0.92k/\omega$. However, the k–ω/k–ϵ blending function (F_1) becomes increasingly important with time, changing from $F_1 = 1$ everywhere at $A_{22}t = 0$ (purely k–ω) to a minimum of 0.55 (at the channel centerline) at $A_{22} = 0.77$ (with the pure k–ω region limited to $y_w < 0.3h$). While discussing the k–ω model we mention that a new version proposed by Wilcox [10] (designed primarily to improve performance in free shear flows) also gives a reasonable $\tau_w = 0$ value, of $A_{22} = 0.55$; the version of k–ω incorporated into the SST scheme [16] yields $A_{22}t = 0.65$ when acting alone (regardless of whether the grid-independent ω boundary condition of Wilcox [16], or that advocated by Menter [14], is used.) Another closure (results not

shown) that performs well is the Johnson–King half-equation model (for which $\tau_w = 0$ at $A_{22}t = 0.60$) – even though, like Cebeci–Smith and BL, it assumes a full-wake external boundary-layer structure. The modified Gulaev ν_T-transport model of Secundov et al. [31] does even better [32], giving a τ_w history closer to the DNS than either SA or SST.

The ability of the four subject models to account for the influence of the APG upon first- and second-order statistics at various wall-normal locations is revealed in Figs. 11–13. Mean velocity[4] profiles are shown at $A_{22}t = 0.365$ and 0.77, and

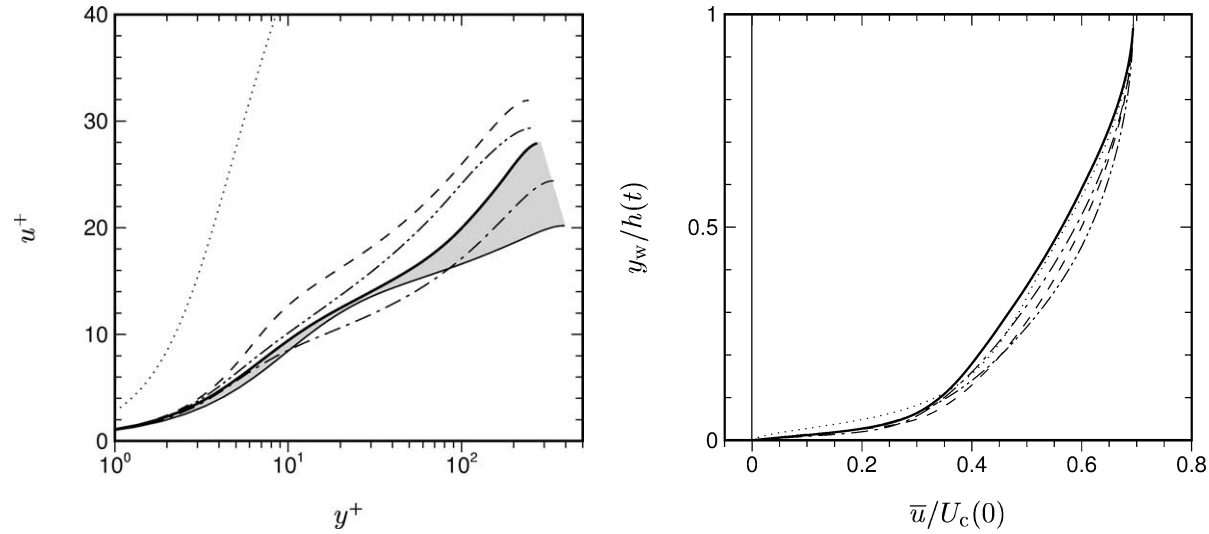

Fig. 11. DNS and model predictions of mean velocity in (a) inner and (b) outer scaling at $A_{22}t = 0.365$: —, DNS; ⋯, BL; - - -, SA; – · –, LS; – ⋯ –, SST. Shaded region in (a) indicates change of DNS from unstrained initial conditions, denoted by thin-solid (—) curve.

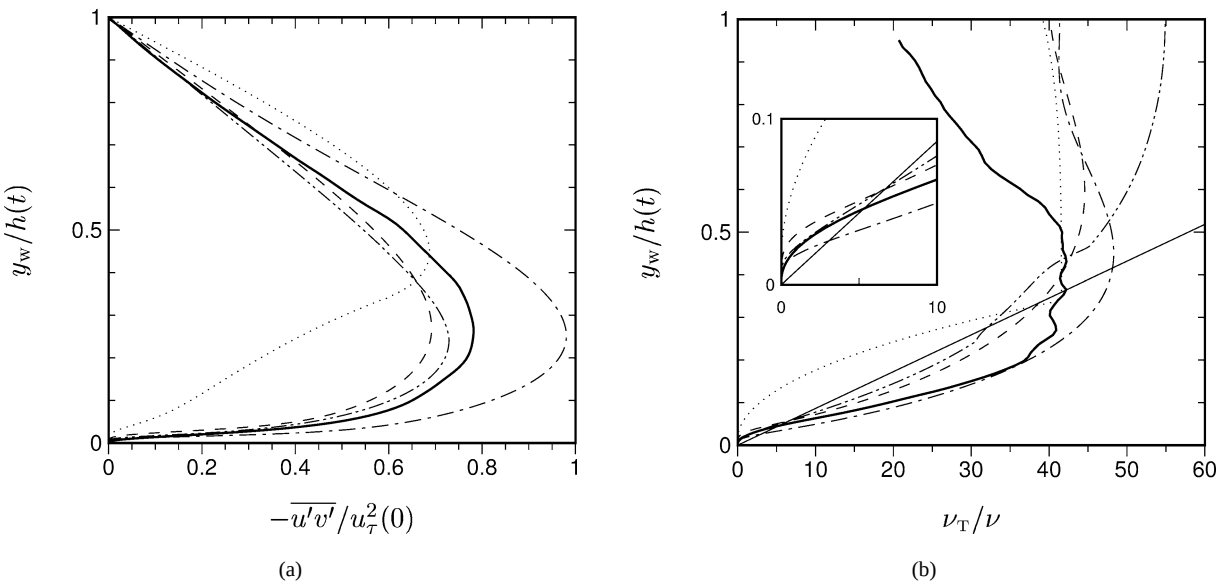

Fig. 12. DNS and model predictions of (a) Reynolds shear stress and (b) eddy viscosity at $A_{22}t = 0.365$: —, DNS; ⋯, BL; - - -, SA; – · –, LS; – ⋯ –, SST. Straight-line segment in (b) denotes $\nu_T = \kappa y_w u_\tau$ from DNS (using $\kappa = 0.41$).

[4] To facilitate comparison with spatial APG boundary layers, the mean velocities in Figs. 11 and 13, and Tables 2 and 3, are presented with respect to the frame of reference attached to the moving channel walls, discussed above. Note the agreement of $U_c(t)/U_c(0)$ between each of the model predictions and the DNS, produced by the moving-wall boundary condition (2).

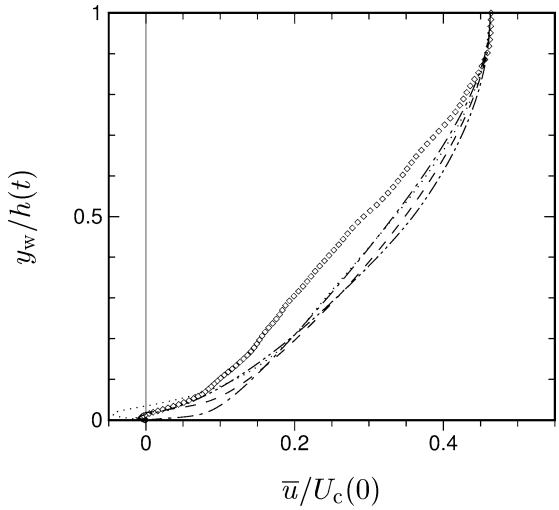

Fig. 13. DNS and model predictions of mean velocity at $A_{22}t = 0.77$: ⋄, DNS (single realization); ⋯, BL; ---, SA; −·−, LS; −⋯−, SST.

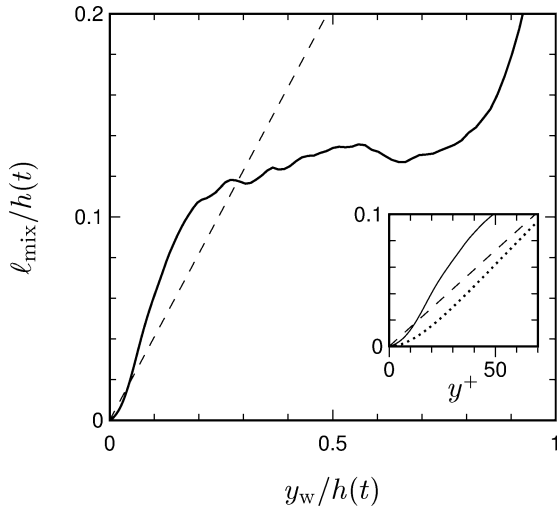

Fig. 14. Mixing-length profiles at $A_{22}t = 0.365$: —, DNS; ---, κy_w ($\kappa = 0.41$); ⋯, $\kappa y_w(1 - \exp(-y_w/A_0^+))$, with $\kappa = 0.41$ and $A_0^+ = 26$.

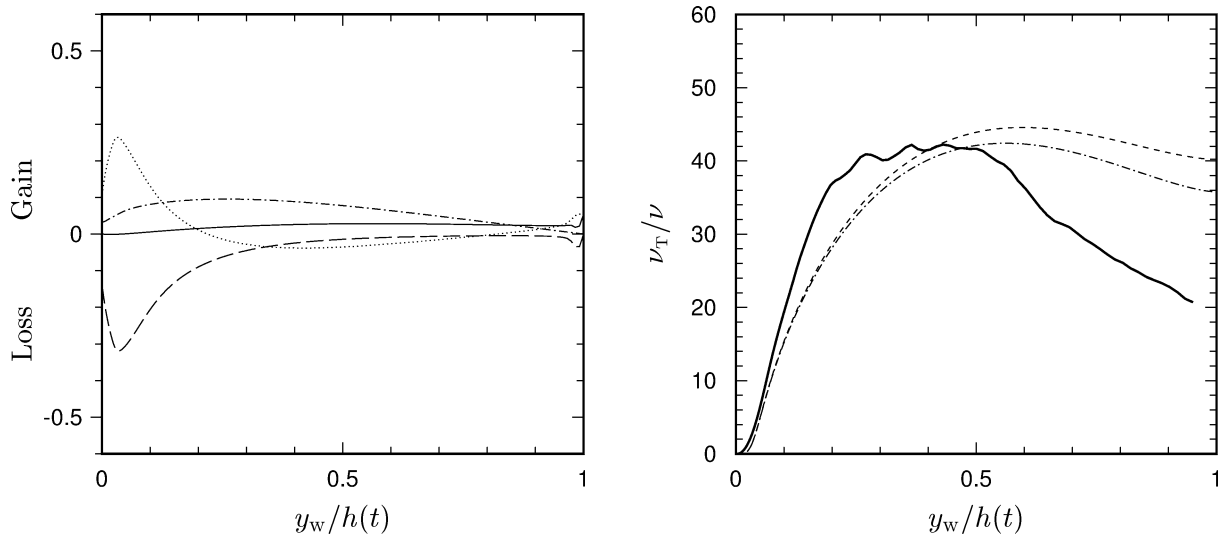

Fig. 15. (a) Terms in SA budget at $A_{22}t = 0.365$: −·−, production; −−−, destruction; ⋯, diffusion; —, $\partial\tilde{\nu}/\partial t$ (see Appendix). (b) Profiles of ν_T at $A_{22}t = 0.365$: —, DNS; ---, SA; −·−, SA with modified distance-to-wall $\mathcal{D} = (2h/\pi)\sin(\pi y_w/2h)$ in destruction term.

Reynolds shear stress and eddy viscosity profiles at $A_{22}t = 0.365$. The shaded region in Fig. 11(a) illustrates the change of the DNS velocity from $A_{22}t = 0$ to 0.365 (see also [2]), implying that the strain induces a 'general' rather than a 'progressive' departure [33,34] from the logarithmic law of the wall – another indication of the challenge faced by RANS models applied to this flow. None of the models achieve engineering accuracy at $A_{22}t = 0.77$; the velocity profiles suffer from excess eddy viscosity near the centerline. Closer to the wall, the eddy viscosity for the DNS (and all but the BL model) also exceeds the law-of-the-wall version of the mixing-length expression, $\kappa y_w u_\tau$ (given by the straight solid line in Fig. 12(b)). This is in contrast to the near-wall region for the unstrained case, where $\kappa y_w u_\tau$ is everywhere an upper bound on ν_T (Fig. 5(b)). It is also consistent with the (slight) downward shift in the log law observed in Spalart and Watmuff's APG flow [5] (since in an APG, where $-\overline{u'v'}/u_\tau^2 > 1$ away from the wall, a decrease in u^+ – and hence du^+/dy^+ – implies ν_T/ν must be greater than κy^+). The maximum eddy viscosity from each of the schemes increases compared to its initial value although modestly, as it does

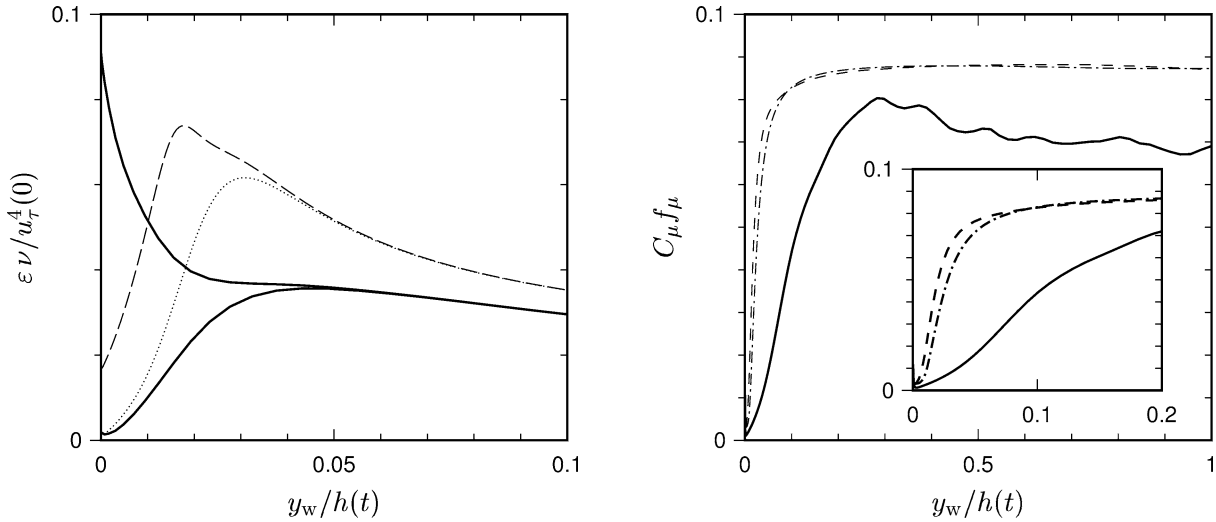

Fig. 16. (a) Dissipation rate ε profiles for LS at $A_{22}t = 0.365$: $\cdots$, $\tilde{\varepsilon}$; $---$, ε; —, $\tilde{\varepsilon}$ and ε from DNS. (b) Eddy-viscosity damping for LS at $A_{22}t = 0.365$: —, $\nu_T\tilde{\varepsilon}/k^2$ from DNS; ---, $C_\mu \exp(-3.4/(1 + \mathrm{Re_T}/50)^2)$, using $\mathrm{Re_T} = k^2/\tilde{\varepsilon}\nu$ from DNS; $-\cdot-$, $C_\mu \exp(-3.4/(1 + \mathrm{Re_T}/50)^2)$, using $\mathrm{Re_T} = k^2/\tilde{\varepsilon}\nu$ from k and $\tilde{\varepsilon}$ predicted by LS. The LS variable $\tilde{\varepsilon} \equiv \varepsilon - \varepsilon_0$ with $\varepsilon_0 = 2\nu(\partial k^{1/2}/\partial y)^2$.

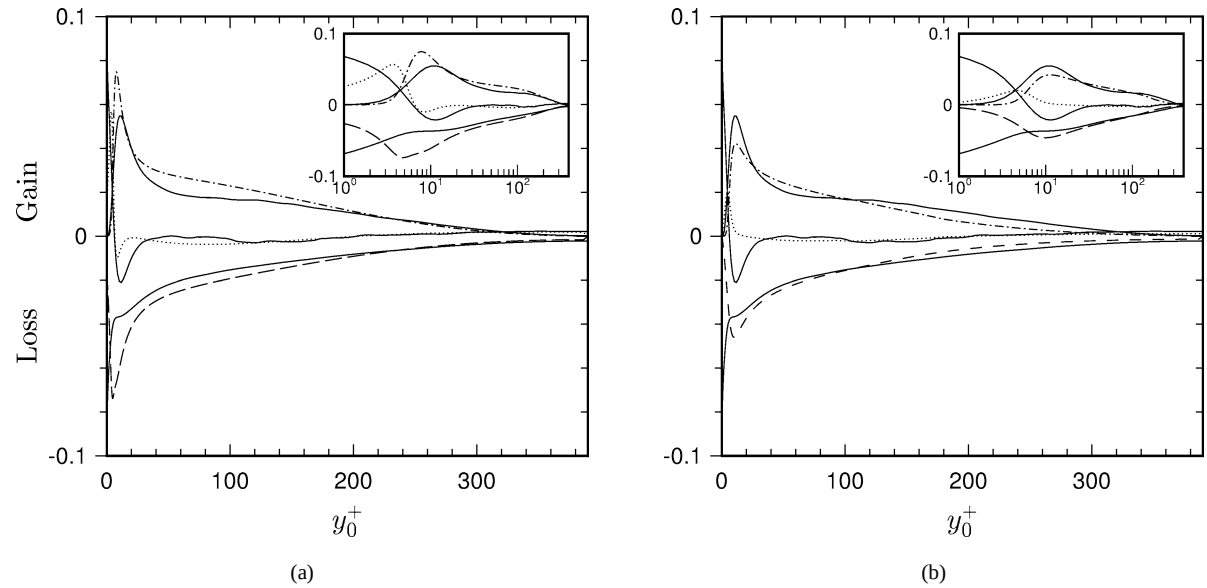

Fig. 17. Terms in turbulence kinetic energy budget for (a) LS and (b) SST at $A_{22}t = 0.365$: $-\cdot-$, production $P_k^S + P_k^A$; $---$, dissipation $-\varepsilon$; $\cdots$, diffusion $T_k + D_k + \Pi_k$; —, DNS. See Fig. 3 caption for definition of budget terms. Curves normalised by $u_\tau^4(0)/\nu$. $y_0^+ = y_w \exp(-A_{22}t)u_\tau(0)/\nu$.

in the DNS (cf. Figs. 5(b) and 12(b)), and in the DNS the effective Clauser coefficient α_{eff} decreases, from $\alpha_{\mathrm{eff}} = 0.0305$ at $A_{22}t = 0$ to $\alpha_{\mathrm{eff}} = 0.023$ at $A_{22}t = 0.365$. The quantitative agreement of the models with the DNS is once again, however, not particularly good. For example, although $\nu_{T,\max}$ from the BL solution is very close to that from the DNS, the profiles are significantly different everywhere else. The correlation between the accuracy of the $\tau_w = 0$ time and the magnitude of the near-wall ν_T is apparent, with the expected early or late separation associated with too-low or too-high values, respectively. The best overall prediction of the $-\overline{u'v'}$ profile is given by the SA and SST models, although both leave room for improvement.

Baldwin–Lomax appears to be primarily a 'victim' of the van Driest damping. The breakdown of the mixing-length hypothesis in the inertial layer (i.e., the assumption that $\ell_{\text{mix}} \approx \kappa y_{\text{w}}$), and the large error associated with assuming $A^+ = 26$, is revealed in Fig. 14.

The terms in the SA budget are shown in Fig. 15(a). The production (proportional to $\nu_{\text{T}} \cdot (\partial \bar{u}/\partial y)$ and thus $-\overline{u'v'}$) is everywhere greater than the sum of the destruction and diffusion, causing net positive $\partial \nu_{\text{T}}/\partial t$ across the channel, as it should. (Although less important than for the $A_{22}t = 0$ flow, the finite f_w and its nonzero contribution to the destruction term at the centerline is again evident.) As with the unstrained case, replacing y_{w} in the destruction term with the quarter-sine approximation to the Fares–Schröder distance function $\mathcal{D}$ causes little change to its magnitude (which is proportional to $(\nu_{\text{T}}/\mathcal{D})^2$). Consequently, this again reduces and thereby improves the SA prediction of ν_{T} in the outer layer – although the improvement is smaller than for the steady/unstrained flow.

The LS diagnostics in Figs. 16 and 17(a) imply that the excess near-wall ν_{T} prediction (Fig. 12(b) inset) is due to the $C_\mu f_\mu$ product in the $\nu_{\text{T}} = C_\mu f_\mu k^2/\tilde{\varepsilon}$ formula being too large, since below $y_{\text{w}} = 0.1h$ the LS k variation (not shown) is less than the $A_{22}t = 0.365$ DNS result (Fig. 2(a)), and since the LS $\tilde{\varepsilon}$ (dotted curve) is much larger than the corresponding DNS values (Fig. 16(a)). (The f_μ damping also contributes to the too-large $\tilde{\varepsilon}$, via the $\tilde{\varepsilon}$ production term.) From Fig. 16(b) we see that C_μ would need to be reduced, and f_μ adjusted so that it approaches zero near the wall with a less steep slope, for LS to match the DNS data.

The model–DNS mismatch in the production terms in Fig. 17 (a) and (b) is consistent with the over- and under-prediction of the peak $-\overline{u'v'}$ respectively given by LS and SST (Fig. 12(a)). However, as shown in Fig. 12(b), for the SST closure this is not accompanied by a serious inaccuracy in the near-wall variation of ν_{T}.

4. Summary and conclusions

A temporally evolving strained plane-channel flow was used as an idealised turbulent APG boundary layer to test the Baldwin–Lomax (BL), Spalart–Allmaras (SA), Launder–Sharma (LS) and Menter SST models, by comparing predictions with direct numerical simulation (DNS) results. The strained-channel flow provides a nontrivial challenge to the models, and produces behaviour similar to that found in actual spatial APG boundary layers. This agreement implies that the strained-channel DNS captures at least the 'first-order' APG effects found in more complex cases. Given its simplicity (a mean flow governed by an unsteady one-dimensional problem), and the detailed information (such as Reynolds-stress budgets) available from the DNS, we expect that this flow will be useful for testing and development of aerospace turbulence models. The data and modeling codes are available to any who may wish to use them.

The unstrained plane channel flow at $\text{Re}_\tau = 390$ was also examined. All four models give fairly accurate skin friction values for this case, although their outer-layer profiles of eddy-viscosity ν_{T} markedly deviate from the DNS data. For BL, the approximately constant ν_{T} associated with the wake component is too small, implying a significantly larger outer-layer Clauser coefficient α is appropriate when two-layer algebraic models are applied to channel/duct flows. The too-large ν_{T} given by SA in the outer layer can be alleviated by altering the destruction term, increasing its magnitude by replacing the distance to the nearest wall with a generalised distance function that takes both walls into account. The major inaccuracy in the LS formation of ν_{T} is excessive dissipation (rather than excessive wall damping, as previously suggested). However, despite this and other inconsistencies between the DNS and the modeling assumptions, the errors compensate such that the LS representation of mean velocity and shear stress (and therefore turbulence kinetic energy production) is good. The same is true for SST, in that its production term is close to that from the DNS, despite large differences between the model and DNS profiles of the other terms (diffusion and dissipation) in the energy budget.

The accuracy of the models is much more varied when applied to the unsteady strained-channel flow. The SA and SST schemes give the best prediction of 'separation' (i.e., the time at which the wall-shear stress becomes negative), with the SST value being within the estimated uncertainty of the DNS results. Both models also yield more accurate Reynolds-stress profiles than BL and LS do, despite fairly large outer-layer deviations of eddy viscosity from the DNS benchmark. The models reveal the same inconsistencies observed for the unstrained flow, which when the strain is applied become more pronounced. For example, for SA, the outer-layer ν_{T} surplus can again be reduced by using a generalised nearest-wall distance function in the destruction term, while for LS the dissipation is again too large and the eddy-viscosity damping f_μ again falls to zero too slowly approaching the wall. (The LS C_μ is also too large.) Although the agreement with DNS for the production term is not particularly good for either LS or SST (and reflects the quality of the Reynolds-stress prediction for each), it is much better than that found for the dissipation and diffusion – another demonstration of how errors can compensate so that the net accuracy of a model is not necessarily defined by the precision of its individual components.

Based on preliminary tests with the second-order stress-ω model [10], we anticipate that capturing this flow will also be well within the capabilities of Reynolds-stress transport models, presumably because of their explicit treatment of the production terms. Nevertheless, in light of the comparable SA and SST performance, and the extra complexity of the (two-equation) SST

closure, a case could be made that the one-equation SA solution represents the optimal accuracy per unit cost for 2D APG applications. (The lesser-known one-equation model of Gulyaev et al. also performs similarly well.) The degree to which these findings are affected by Reynolds number and strength of the APG strain is at present unknown, and will be the topic of future studies.

Acknowledgements

This work was supported by the UK Engineering and Physical Sciences Research Council (Grant GR/N20249) and in part by the LMFA, École Centrale de Lyon. The authors are grateful to Dr. Dennis Johnson, Prof. Neil Sandham and especially Dr. Philippe Spalart for their comments and suggestions.

Appendix. Model equations for APG strained-channel flow

For future reference, we consider the most general case produced by applying a steady uniform irrotational divergence-free deformation to a parallel plane-channel flow, with nonzero streamwise acceleration/deceleration A_{11}, wall-normal divergence/convergence A_{22} and lateral convergence/divergence A_{33},

$$A_{ij} \equiv \frac{\partial U_i}{\partial x_j} = \begin{bmatrix} \partial U/\partial x & 0 & 0 \\ 0 & \partial V/\partial y & 0 \\ 0 & 0 & \partial W/\partial z \end{bmatrix}, \tag{4}$$

where

$$A_{ii} = A_{11} + A_{22} + A_{33}.$$

We assume the A_{22} component is orthogonal to the plane walls, and allow for the possibility that both the streamwise $\bar{u}$ and spanwise $\overline{w}$ components of the mean velocity of the channel flow to which this strain is applied are nonzero. When $\overline{w} \neq 0$ and either A_{11} or A_{33} are nonzero, this produces irrotational skewing, when viewed in a coordinate system aligned with the mean velocity vector $(\bar{u}, \overline{w})$; see [4] for details.

The mean momentum equations and the four eddy-viscosity closure schemes will be written in terms of a Lagrangian coordinate system that deforms under the influence of the applied rate of wall-normal strain A_{22}. In this system the independent variables (η, λ) are given by $\eta(y,t) = \exp(-A_{22}t)y = b(t)y$ and $\lambda(y,t) = t$. (The streamwise and spanwise components of the deforming coordinate need not be considered here, since we are only concerned with equations governing the mean statistics, which vary only in the wall-normal direction and time.)

After making the eddy-viscosity assumption, the $\bar{u}$ and $\overline{w}$ transport equations are respectively

$$\frac{\partial \bar{u}}{\partial \lambda} = -A_{11}\bar{u} + b^2(\lambda)\frac{\partial}{\partial \eta}\left[(\nu + \nu_{\mathrm{T}})\frac{\partial \bar{u}}{\partial \eta}\right], \tag{5}$$

$$\frac{\partial \overline{w}}{\partial \lambda} = -A_{33}\overline{w} + b^2(\lambda)\frac{\partial}{\partial \eta}\left[(\nu + \nu_{\mathrm{T}})\frac{\partial \overline{w}}{\partial \eta}\right], \tag{6}$$

where $b(\lambda) = \exp(-A_{22}\lambda)$. The boundary conditions are $\bar{u}(\eta,\lambda) = U_{\mathrm{w}}(\lambda)$ and $\overline{w}(\eta,\lambda) = W_{\mathrm{w}}(\lambda)$ at $\eta = \pm h(0)$, where the streamwise and spanwise wall velocities are adjusted dynamically, based on the initial and current values of the mean centerline velocity $(U_{\mathrm{c}}, W_{\mathrm{c}})$:

$$U_{\mathrm{w}}(\lambda) = U_{\mathrm{c}}(\lambda) - U_{\mathrm{c}}(0)\exp(A_{11}\lambda) \quad \text{and} \quad W_{\mathrm{w}}(\lambda) = W_{\mathrm{c}}(\lambda) - W_{\mathrm{c}}(0)\exp(A_{33}\lambda). \tag{7}$$

We invoke symmetry and solve Eqs. (5) and (6), and the following model equations, between $\eta = -h(0)$ and 0, or equivalently, in terms of the nearest-wall distance $\eta_{\mathrm{w}} = b(\lambda)y_{\mathrm{w}} = b(\lambda)|h(t) - y|$, between the wall at $\eta_{\mathrm{w}} = 0$ and the channel centerline at $\eta_{\mathrm{w}} = h(0)$. In the half-channel domain, the boundary conditions are

$$\bar{u} = U_{\mathrm{w}} \quad \text{and} \quad \overline{w} = W_{\mathrm{w}} \quad \text{at } \eta_{\mathrm{w}} = 0; \qquad \partial\bar{u}/\partial\eta = \partial\overline{w}/\partial\eta = 0 \quad \text{at } \eta_{\mathrm{w}} = h(0).$$

Details of the four eddy-viscosity models considered in this paper are listed below; they were solved using the finite-difference scheme described in Section 2.1, for the 2D APG case, for which $A_{33} = 0$ and $\overline{w} = W_{\mathrm{c}} = W_{\mathrm{w}} = 0$.

- Baldwin–Lomax (BL) (1978) algebraic model [9,10]:

Eddy viscosity:

$$\nu_{\mathrm{T}} = \begin{cases} \overline{\omega}\ell_{\mathrm{mix}}^2 & \text{if } \eta_{\mathrm{w}} \leqslant \eta_{\max}, \\ \alpha C_{\mathrm{cp}} F_{\mathrm{wake}} F_{\mathrm{Kleb}}(\eta_{\mathrm{w}}/\eta_{\max}) & \text{if } \eta_{\mathrm{w}} > \eta_{\max}. \end{cases} \tag{8}$$

Auxiliary functions:

$$\overline{\omega}^2 = b^2(\lambda)\left(\frac{\partial \bar{u}}{\partial \eta}\right)^2 + b^2(\lambda)\left(\frac{\partial \overline{w}}{\partial \eta}\right)^2, \qquad \ell_{\mathrm{mix}} = \kappa\left(\frac{\eta_{\mathrm{w}}}{b(\lambda)}\right)\left[1 - \mathrm{e}^{-y^+/A_0^+}\right],$$

$$y^+ = \frac{\eta_{\mathrm{w}} u_\tau}{\nu b(\lambda)}, \qquad u_\tau^2 = \tau_{\mathrm{w}} = \nu b(\lambda)\left(\frac{\partial \bar{u}}{\partial \eta}\right)_{\mathrm{w}}, \qquad b(\lambda) = \exp(-A_{22}\lambda),$$

$$b(\lambda) F_{\mathrm{wake}} = \min\left[\eta_{\max} F_{\max}, C_{\mathrm{wk}}\eta_{\max}\left[\left(U_{\mathrm{c}}^2 + W_{\mathrm{c}}^2\right)^{1/2} - \left(U_{\mathrm{w}}^2 + W_{\mathrm{w}}^2\right)^{1/2}\right]/F_{\max}\right],$$

$$\kappa F_{\max} = \max[\overline{\omega}\ell_{\mathrm{mix}}], \qquad F_{\mathrm{Kleb}} = 1\Big/\left[1 + 5.5\left(C_{\mathrm{Kleb}}\frac{\eta_{\mathrm{w}}}{\eta_{\max}}\right)^6\right],$$

where $\eta_{\max}$ is η_{w} at which $F_{\max}$ is evaluated.
Constants:

$$A_0^+ = 26, \quad \kappa = 0.4, \quad \alpha = 0.0168, \quad C_{\mathrm{cp}} = 1.6, \quad C_{\mathrm{Kleb}} = 0.3, \quad C_{\mathrm{wk}} = 1.$$

- Spalart–Allmaras (SA) (1994) one-equation/ν_{T}-transport model [11,12,10]:
Eddy viscosity:

$$\nu_{\mathrm{T}} = \tilde{\nu} f_{v1}. \tag{9}$$

Transport equation:

$$\frac{\partial \tilde{\nu}}{\partial \lambda} = C_{\mathrm{b1}}\widetilde{S}\tilde{\nu} - C_{\mathrm{w1}}\left[\frac{\tilde{\nu} b(\lambda)}{\eta_{\mathrm{w}}}\right]^2 f_w + \frac{b^2(\lambda)}{\sigma}\left[\frac{\partial}{\partial \eta}\left[(\nu + \tilde{\nu})\frac{\partial \tilde{\nu}}{\partial \eta}\right] + C_{\mathrm{b2}}\left(\frac{\partial \tilde{\nu}}{\partial \eta}\right)^2\right]. \tag{10}$$

Boundary conditions:

$$\tilde{\nu} = 0 \quad \text{at } \eta_{\mathrm{w}} = 0; \qquad \frac{\partial \tilde{\nu}}{\partial \eta} = 0 \quad \text{at } \eta_{\mathrm{w}} = h(0).$$

Auxiliary functions:

$$\widetilde{S} = S + \frac{b^2(\lambda)\tilde{\nu}}{\kappa^2 \eta_{\mathrm{w}}^2} f_{v2}, \qquad S = b^2(\lambda)\left(\frac{\partial \bar{u}}{\partial \eta}\right)^2 + b^2(\lambda)\left(\frac{\partial \overline{w}}{\partial \eta}\right)^2, \qquad b(\lambda) = \exp(-A_{22}\lambda),$$

$$f_{v1} = \frac{\chi^3}{\chi^3 + C_{\mathrm{v1}}^3}, \qquad f_{v2} = 1 - \frac{\chi}{1 + \chi f_{v1}}, \qquad \chi = \frac{\tilde{\nu}}{\nu},$$

$$f_w = g\left[\frac{1 + C_{\mathrm{w3}}^6}{g^6 + C_{\mathrm{w3}}^6}\right]^{1/6}, \qquad g = r + C_{\mathrm{w2}}\left(r^6 - r\right), \qquad r = \frac{\tilde{\nu} b^2(\lambda)}{\widetilde{S}\kappa^2 \eta_{\mathrm{w}}^2}.$$

Constants:

$$C_{\mathrm{b1}} = 0.1355, \quad \sigma = 2/3, \quad C_{\mathrm{b2}} = 0.622, \quad \kappa = 0.41, \quad C_{\mathrm{v1}} = 7.1,$$

$$C_{\mathrm{w1}} = \frac{C_{\mathrm{b1}}}{\kappa^2} + \frac{1 + C_{\mathrm{b2}}}{\sigma} \approx 3.239, \quad C_{\mathrm{w2}} = 0.3, \quad C_{\mathrm{w3}} = 2.$$

- Launder–Sharma (LS) (1974) low-Reynolds-number two-equation/k–ε model [13,12,10]:
Eddy viscosity:

$$\nu_{\mathrm{T}} = C_\mu f_\mu \frac{k^2}{\tilde{\varepsilon}}. \tag{11}$$

Transport equations:

$$\frac{\partial k}{\partial \lambda} = \nu_{\mathrm{T}}\left[b^2(\lambda)\left(\frac{\partial \bar{u}}{\partial \eta}\right)^2 + b^2(\lambda)\left(\frac{\partial \overline{w}}{\partial \eta}\right)^2 + 2\left(A_{11}^2 + A_{22}^2 + A_{33}^2\right)\right] - \varepsilon + b^2(\lambda)\frac{\partial}{\partial \eta}\left[\left(\nu + \frac{\nu_{\mathrm{T}}}{\sigma_k}\right)\frac{\partial k}{\partial \eta}\right], \tag{12}$$

$$\frac{\partial \tilde{\varepsilon}}{\partial \lambda} = C_{\epsilon 1} f_1 \frac{\tilde{\varepsilon}}{k}\nu_{\mathrm{T}}\left[b^2(\lambda)\left(\frac{\partial \bar{u}}{\partial \eta}\right)^2 + b^2(\lambda)\left(\frac{\partial \overline{w}}{\partial \eta}\right)^2 + 2\left(A_{11}^2 + A_{22}^2 + A_{33}^2\right)\right] - C_{\epsilon 2} f_2 \frac{\tilde{\varepsilon}}{k} + E + b^2(\lambda)\frac{\partial}{\partial \eta}\left[\left(\nu + \frac{\nu_{\mathrm{T}}}{\sigma_\epsilon}\right)\frac{\partial \tilde{\varepsilon}}{\partial \eta}\right]. \tag{13}$$

Boundary conditions:

$$k = \tilde{\varepsilon} = 0 \quad \text{at } \eta_{\mathrm{w}} = 0; \qquad \frac{\partial k}{\partial \eta} = \frac{\partial \tilde{\varepsilon}}{\partial \eta} = 0 \quad \text{at } \eta_{\mathrm{w}} = h(0).$$

Auxiliary functions:

$$\varepsilon = \varepsilon_0 + \tilde{\varepsilon}, \quad \varepsilon_0 = 2\nu b^2(\lambda)\left(\frac{\partial^2 k^{1/2}}{\partial \eta^2}\right)^2, \quad E = 2\nu\nu_{\mathrm{T}} b^4(\lambda)\left(\frac{\partial^2 \bar{u}}{\partial \eta^2}\right)^2, \quad b(\lambda) = \exp(-A_{22}\lambda),$$

$$f_\mu = \mathrm{e}^{-3.4/(1+\mathrm{Re_T}/50)^2}, \quad f_1 = 1, \quad f_2 = 1 - 0.3\,\mathrm{e}^{-\mathrm{Re_T^2}}, \quad \mathrm{Re_T} = k^2/\tilde{\varepsilon}\nu.$$

Constants:

$$C_\mu = 0.09, \quad C_{\epsilon 1} = 1.44, \quad C_{\epsilon 2} = 1.92, \quad \sigma_k = 1, \qquad \sigma_\epsilon = 1.3.$$

- Shear-Stress Transport (SST) two-equation model (Menter 1994) [14,12]:
Eddy viscosity:

$$\nu_{\mathrm{T}} = \frac{k/\omega}{\max[1, \Omega F_2/a_1\omega]}. \tag{14}$$

Transport equations:

$$\frac{\partial k}{\partial \lambda} = \nu_{\mathrm{T}}\left[b^2(\lambda)\left(\frac{\partial \bar{u}}{\partial \eta}\right)^2 + b^2(\lambda)\left(\frac{\partial \overline{w}}{\partial \eta}\right)^2 + 2\left(A_{11}^2 + A_{22}^2 + A_{33}^2\right)\right] - \beta^* k\omega + b^2(\lambda)\frac{\partial}{\partial \eta}\left[(\nu + \hat{\sigma}_k \nu_{\mathrm{T}})\frac{\partial k}{\partial \eta}\right], \tag{15}$$

$$\frac{\partial \omega}{\partial \lambda} = \hat{\gamma}\left[b^2(\lambda)\left(\frac{\partial \bar{u}}{\partial \eta}\right)^2 + b^2(\lambda)\left(\frac{\partial \overline{w}}{\partial \eta}\right)^2 + 2\left(A_{11}^2 + A_{22}^2 + A_{33}^2\right)\right] - \hat{\beta}\omega^2 + b^2(\lambda)\frac{\partial}{\partial \eta}\left[(\nu + \hat{\sigma}_\omega \nu_{\mathrm{T}})\frac{\partial \omega}{\partial \eta}\right] + 2(1 - F_1)\frac{\sigma_{\omega 2}}{\omega} b^2(\lambda)\frac{\partial k}{\partial \eta}\frac{\partial \omega}{\partial \eta}. \tag{16}$$

Boundary conditions:

$$k = 0 \quad \text{and} \quad \omega = \frac{60\nu b^2(\lambda)}{\beta_1 \Delta\eta_0^2} \quad \text{at } \eta_{\mathrm{w}} = 0; \qquad \frac{\partial k}{\partial \eta} = \frac{\partial \omega}{\partial \eta} = 0 \quad \text{at } \eta_{\mathrm{w}} = h(0),$$

where $\beta_1 = 0.075$ and $\Delta\eta_0$ is the distance from the wall to the first grid point, which must be less than $\sqrt{b(\lambda)\nu/(\partial \bar{u}/\partial \eta)_{\mathrm{w}}}$ (see [12,10]).
Auxiliary functions:

$$\Omega^2 = b^2(\lambda)\left(\frac{\partial \bar{u}}{\partial \eta}\right)^2 + b^2(\lambda)\left(\frac{\partial \overline{w}}{\partial \eta}\right)^2, \qquad b(\lambda) = \exp(-A_{22}\lambda),$$

$$F_2 = \tanh\left\{\left[\max(2g_1, g_2)\right]^2\right\}, \qquad F_1 = \tanh\left\{\left\langle\left[\max(g_1, g_2), g_3\right]\right\rangle^4\right\},$$

$$g_1 = \frac{k^{1/2} b(\lambda)}{0.09\omega\eta_{\mathrm{w}}}, \quad g_2 = \frac{500\nu b^2(\lambda)}{\omega\eta_{\mathrm{w}}^2}, \quad g_3 = \frac{4\sigma_{\omega 2} k b^2(\lambda)}{\Psi\eta_{\mathrm{w}}^2}, \quad \Psi = \max\left[\frac{2\sigma_{\omega 2}}{\omega} b^2(\lambda)\frac{\partial k}{\partial \eta}\frac{\partial \omega}{\partial \eta}, 10^{-20}\right].$$

Constants:

$$a_1 = 0.31, \qquad \beta^* = 0.09.$$

Blending constants:
The blending function F_1 is used to determine $\hat{\sigma}_k$, $\hat{\sigma}_\omega$, $\hat{\beta}$, and $\hat{\gamma}$ in (15) and (16), according to

$$\hat{\phi} = F_1\phi_1 + (1 - F_1)\phi_2 \quad \text{where } \hat{\phi} = (\hat{\sigma}_k, \hat{\sigma}_\omega, \hat{\beta}, \hat{\gamma}),$$

and ϕ_1 and ϕ_2 denote respectively the inner (k–ω) and ϕ_2 the outer (k–ϵ) constants:

$$(\sigma_{k1}, \sigma_{\omega 1}, \beta_1, \gamma_1) = (0.85, 0.5, 0.075, 0.553) \quad \text{and} \quad (\sigma_{k2}, \sigma_{\omega 2}, \beta_2, \gamma_2) = (1, 0.856, 0.0828, 0.440).$$

References

[1] G.N. Coleman, J. Kim, P.R. Spalart, Direct numerical simulation of decelerated wall-bounded shear flows, in: Proceedings of the Eleventh Symposium on Turbulent Shear Flows, September 1997, 33-1–33.6.
[2] G.N. Coleman, J. Kim, P.R. Spalart, Direct numerical simulation of a decelerated wall-bounded turbulent shear flow, J. Fluid Mech. (2003) in press.
[3] F.R. Menter, Performance of popular turbulence models for attached and separated adverse pressure gradient flows, AIAA J. 30 (1992) 2066–2072.
[4] G.N. Coleman, J. Kim, P.R. Spalart, A numerical study of strained three-dimensional wall-bounded turbulence, J. Fluid Mech. 416 (2000) 75–116.
[5] P.R. Spalart, J.H. Watmuff, Experimental and numerical study of a turbulent boundary layer with pressure gradients, J. Fluid Mech. 249 (1993) 337–371.
[6] Y. Nagano, T. Tsuji, T. Houra, Structure of turbulent boundary layer subjected to adverse pressure gradient, in: Proceedings of the Eleventh Symposium on Turbulent Shear Flows, September 1997, 33-7–33.12.
[7] A.E. Alving, H.H. Fernholz, Mean-velocity scaling in and around a mild, turbulent separation bubble, Phys. Fluids 7 (1995) 1956–1969.
[8] W.M. Kays, M.E. Crawford, Convective Heat and Mass Transfer, Third edition, McGraw-Hill, 1993.
[9] B.S. Baldwin, H. Lomax, Thin-layer approximation and algebraic model for separated turbulent flows, AIAA Paper 78-257, 1978.
[10] D.C. Wilcox, Turbulence Modeling for CFD, Second edition, DCW Industries, 1998.
[11] P. Spalart, S. Allmaras, A one-equation turbulence model for aerodynamic flows, Rech. Aèrospat. 1 (1994) 5–21.
[12] J.E. Bardina, P.G. Huang, T.J. Coakley, Turbulence modeling validation, testing, and development, NASA Tech. Memo. 110446, April 1997.
[13] B.E. Launder, B.I. Sharma, Application of the energy dissipation model of turbulence to the calculation of flow near a spinning disc, Lett. Heat Mass Transfer 1 (1974) 131–138.
[14] F.R. Menter, Two-equation eddy-viscosity turbulence models for engineering applications, AIAA J. 32 (1994) 1598–1605.
[15] D.A. Johnson, Transonic separated flow predictions with an eddy-viscosity/Reynolds-stress closure model, AIAA J. 25 (1987) 252–259.
[16] D.C. Wilcox, Reassessment of the scale-determining equation for advanced turbulence models, AIAA J. 26 (1988) 1299–1310.
[17] W.P. Jones, B.E. Launder, The prediction of laminarization with a two-equation model of turbulence, Int. J. Heat Mass Transfer 15 (1972) 301–314.
[18] K.-Y. Chien, Predictions of channel and boundary-layer flows with a low-Reynolds-number turbulence model, AIAA J. 20 (1982) 33–38.
[19] T. Cebeci, A.M.O. Smith, Analysis of Turbulent Boundary Layers, Academic Press, 1974.
[20] B.S. Baldwin, T.J. Barth, A one-equation turbulence transport model for high Reynolds number wall-bounded flows, AIAA Paper 91-0610, 1991.
[21] E. Fares, W. Schröder, A differential equation for approximate wall distance, Int. J. Numer. Methods Fluids 39 (2002) 743–762.
[22] P.A. Durbin, B.A. Pettersson Reif, Statistical Theory and Modeling for Turbulent Flows, Wiley, 2001.
[23] R.M. Halleen, J.P. Johnston, The influence of rotation on flow in a long rectangular channel – an experimental study, Report No. MD-18, Dept. Mech. Engrg., Stanford University, CA, 1967.
[24] R.B. Dean, Reynolds number dependence of skin friction and other bulk flow variables in two-dimensional rectangular duct flow, J. Fluid Engrg. 100 (1978) 215–223.
[25] V. Michelassi, W. Rodi, W. Zhu, Testing a low Reynolds number k–ϵ turbulence model based on direct numerical simulation data, AIAA J. 31 (1993) 1720–1723.
[26] H. Schlichting, Boundary-Layer Theory, Seventh edition, McGraw-Hill, 1979.
[27] Z.W. Hu, N.D. Sandham, Large-domain simulations of Couette and Poiseuille flow, in: E. Lindborg, et al. (Eds.), Proceedings of the Second International Symposium on Turbulence and Shear Flow Phenomena, KTH, Sweden, June 2001, pp. 377–382.
[28] G.N. Coleman, J. Kim, P.R. Spalart, Reynolds-stress budgets from a wall-bounded adverse-pressure-gradient flow, in: C. Dopazo, et al. (Eds.), Advances in Turbulence VIII – Proceedings of the Eighth European Turbulence Conference, June 2000, pp. 415–418.
[29] D.M. Driver, Reynolds shear stress measurements in a separated boundary layer, AIAA Paper 91-1787, 1991.
[30] T.L. Holst, Viscous transonic airfoil workshop. Compendium of results, AIAA Paper 91-1787, 1987.
[31] A.N. Secundov, M.Kh. Strelets, A.K. Travin, Generalization of ν_t-92 turbulence model for shear-free and stagnation point flow, J. Fluids Engrg. 123 (2001) 11–15.
[32] A.N. Secundov, Personal communication, 1997.
[33] R.A. McD. Galbraith, S. Sjolander, M.R. Head, Mixing length in the wall region of turbulent boundary layers, Aeronaut. Quart. 28 (1977) 97–110.
[34] P.G. Huang, P. Bradshaw, Law of the wall for turbulent flows in pressure gradients, AIAA J. 33 (1995) 624–632.